NASA/CR-1998- 206682

FINAL
IN-34-CR
13CIT
047 879

Control of
Oscillatory Thermocapillary Convection in Microgravity

(NAG 3-1454)

Final Report

Submitted to:

Dr. Ray Skarda

Microgravity Fluids Branch, Mail Stop 500/102
NASA Lewis Research Center
21000 Brookpark Road
Cleveland, OH 44135

by

Prof. G. Paul Neitzel, Principal Investigator

The George W. Woodruff School of Mechanical Engineering
Georgia Institute of Technology
Atlanta, GA 30332-0405

January, 1998

I. Summary

This project focused on the generation and suppression of oscillatory thermocapillary convection in a thin liquid layer. While the bulk of the research was experimental in nature, some theoretical work was also done.

The first phase of this research generated, for the first time, the hydrothermal-wave instability predicted by Smith and Davis in 1983. In addition, the behavior of the fluid layer under a number of conditions was investigated and catalogued. A transition map for the instability of buoyancy-thermocapillary convection was prepared which presented results in terms of apparatus-dependent and apparatus-independent parameters, for ease of comparison with theoretical results.

The second phase of this research demonstrated the suppression of these hydrothermal waves through an active, feed-forward control strategy employing a CO_2 laser to selectively heat lines of negative disturbance temperature on the free surface of the liquid layer. An initial attempt at this control was only partially successful, employing a thermocouple inserted slightly below the free surface of the liquid to generate the control scheme. Subsequent efforts, however, were completely successful in suppressing oscillations in a portion of the layer by utilizing data from an infrared image of the free surface to compute hydrothermal-wave phase speeds and, using these, to tailor the control scheme to each passing wave.

One Ph.D. student (R. Jeffrey Riley) completed his degree at Georgia Tech under support from this grant. Another student who had been working on the project with additional support from a NASA GSRP fellowship had to leave the program early due to failure to successfully complete the Ph.D. qualifying examinations. Two additional doctoral students (Simon Benz and Peter Hintz) from the laboratory of Professor Dietrich Schwabe at Universität Gießen each spent six months in Atlanta working on this project. Their research on this project will become part of their doctoral theses at Universität Gießen and Professor Neitzel is a member of their doctoral committees there.

Two papers have been accepted for publication in the *Journal of Fluid Mechanics* and will appear in 1998. Corrected preprints of these papers are included as an appendix. The final paper will be a discussion of the results of our experiments in light of several linear-stability analyses (including our own) of the basic state of steady buoyancy-thermocapillary convection. This paper will be submitted for publication in calendar year 1998.

II. Project Personnel

G. Paul Neitzel, Professor, Principal Investigator

R. Jeffrey Riley, Ph. D. Student (dissertation defended December, 1996)

David L. Kiesling, Ph.D. Student (NASA GSRP Fellowship Recipient) (left program Fall quarter, 1994)

Simon Benz, Ph.D. Student, Universität Gießen, Germany (on loan to the project from the laboratory of Professor Dietrich Schwabe)

Peter Hintz, Ph.D. Student, Universität Gießen, Germany (on loan to the project from the laboratory of Professor Dietrich Schwabe)

III. Publications and Presentations

Journal papers

R. J. Riley and G. P. Neitzel, "Instability of Thermocapillary Convection in Shallow Layers. Part 1. Characterization of Steady and Oscillatory Instabilities," *Journal of Fluid Mechanics*, to appear (1998).

S. Benz, P. Hintz R. J. Riley and G. P. Neitzel, "Instability of Thermocapillary Convection in Shallow Layers. Part 2. Suppression of Hydrothermal Waves," *Journal of Fluid Mechanics*, to appear (1998).

R. J. Riley and G. P. Neitzel, "Linear-Stability of Buoyancy-Thermocapillary Convection in Shallow Layers," in preparation.

Conference presentations

R. J. Riley and G. P. Neitzel, "Linear Stability of Combined Thermocapillary-Buoyancy Convection in a Horizontal Slot," presented at the Forty-Fifth Meeting of the Division of Fluid Dynamics of the American Physical Society, Tallahassee, FL, November 22-24, 1992.

R. J. Riley and G. P. Neitzel, "Experiments on Multicellular Thermocapillary-Buoyancy Convection," presented at the Winter Annual Meeting of the American Society of Mechanical Engineers, New Orleans, LA, November 28 - December 3, 1993. In *Surface-Tension-Driven Flows*, G. P. Neitzel and M. K Smith, eds., AMD-Vol. 170, American Society of Mechanical Engineers, New York (1993), 75-88. (with).

G. P. Neitzel, and R. J. Riley, "Steady, Multicellular Flow of Combined Thermocapillary-Buoyancy Convection in a Shallow Horizontal Slot," presented at the Forty-Sixth Meeting of the Division of Fluid Dynamics of the American Physical Society, Albuquerque, NM, November 21-23, 1993.

G. P. Neitzel, "Control of Oscillatory Thermocapillary Convection in Microgravity," presented at the Second Microgravity Fluid Physics Conference, Cleveland, OH, June 21-23, 1994.

R. J. Riley, and G. P. Neitzel, "Hydrothermal-Wave and Steady, Multicellular Instability of a Thermocapillary-Buoyancy Driven Flow," presented at the Forty-Seventh Meeting of the Division of Fluid Dynamics of the American Physical Society, Atlanta, GA, November 20-22, 1994.

R. J. Riley, and G. P. Neitzel, "Control of Hydrothermal Wave Instabilities in a Thermocapillary-Driven Flow," presented at the Forty-Eighth Meeting of the Division of Fluid Dynamics of the American Physical Society, Irvine, CA, November 19-21, 1995.

R. J. Riley, and G. P. Neitzel, "Control of Oscillatory Thermocapillary Convection," presented at the Second European Symposium on Fluids in Space, Naples, Italy, April 22-26, 1996.

S. Benz, P. Hintz and G. P. Neitzel, "Improved Active Control of Hydrothermal Wave Instabilities," presented at the Forty-Ninth Meeting of the Division of Fluid Dynamics of the American Physical Society, Syracuse, NY, November 24-26, 1996.

G. P. Neitzel, S. Benz, P. Hintz and R. J. Riley, "Suppression of Oscillatory Thermocapillary Convection in Thin Liquid Layers," *invited* paper (AIAA-97-2119) presented at the 28th AIAA Fluid Dynamics Conference/4th AIAA Shear Flow Control Conference, Snowmass Village, CO, June 29 - July 2, 1997

G. P. Neitzel, "Thermocapillary Convection in Microgravity," *invited* talk presented at JASMAC-13 (proceedings, pp. 17-20), Meeting of the Japan Society of Microgravity Application, Fukuoka, Japan, October 30-31, 1997

Research seminars presented at the following universities:

Stanford University, March 6, 1992

Universität Gießen, July 11, 1994

University of Alabama in Huntsville, October 16, 1997

MARS Center, Naples (Italy), October 9, 1992

University of Florida, January 25, 1993

Massachusetts Institute of Technology, March 7, 1994

Clarkson University, March 21, 1994

Université d'Aix-Marseille II, July 8, 1994

University of Kentucky, October 7, 1994

University of Virginia, April 13, 1995

The Pennsylvania State University, February 2, 1996

Emory University, September 13, 1996

Moscow State University (Russia), November 21, 1996

University of North Carolina at Charlotte, October 14, 1997

Appendix

Preprints of Journal Papers

T4052
H19834 fm
23 pages

J. Fluid Mech. (1998), vol. 35X, pp. 1–23. Printed in the United Kingdom

Instability of thermocapillary–buoyancy convection in shallow layers. Part 1. Characterization of steady and oscillatory instabilities

By R. J. RILEY† AND G. P. NEITZEL

The George W. Woodruff School of Mechanical Engineering, Georgia Institute of Technology,
Atlanta, GA 30332-0405, USA

(Received 5 October 1996 and in revised form 12 November 1997)

Combined thermocapillary–buoyancy convection in a thin rectangular geometry is investigated experimentally, with an emphasis on the generation of hydrothermal-wave instabilities. For sufficiently thin layers, pure hydrothermal waves are observed, and are found to be oblique as predicted by a previous linear-stability analysis (Smith & Davis 1983). For thicker layers, both a steady multicell state and an oscillatory state are found to exist, but the latter is not in the form of a pure hydrothermal wave.

1. Introduction

Thermocapillary convection is bulk fluid motion driven by temperature-induced interfacial-tension variations. Such flows occur in situations with liquid–liquid or liquid–gas interfaces which also experience variations in temperature. The case of interest is that of a free surface between a liquid and a passive gas. For liquids of interest here, surface tension decreases with increasing temperature, and this effect is represented by the fluid property $\gamma = -\partial\sigma/\partial T$, where σ is the surface tension and T is the temperature of the interface. Through the tangential-stress balance at the interface, surface-temperature gradients generate an interfacial shear stress which drives the surface flow in the direction opposite to that of the surface-temperature gradient. For thermally driven flows, buoyancy forces will also be present, but if the dimensions of the flow are small enough or if the flow occurs in a microgravity environment, thermocapillary forces will be dominant. Examples of such flows include the thermocapillary migration of small bubbles or droplets in a thermal field, and classical Rayleigh–Bénard convection.

Recently, there has been interest in the role of thermocapillary convection in processes such as thin-film coating and crystal growth from the melt. Specifically, in crystal-growth flows there is interest in the instability of steady thermocapillary convection, leading to oscillatory convection which results in poor crystal quality brought about by unsteady solidification at the liquid/crystal (freezing) interface (Gatos 1982). To this end there has been a large amount of research done on a model of the float-zone crystal-growth process known as the half-zone. In this model, a liquid bridge is held in place by surface-tension forces between two coaxial cylindrical rods maintained at different temperatures. Buoyancy is minimized by heating the half-zone

† Present address: Cabot Corporation, Research and Development, Pampa, TX 79066, USA.

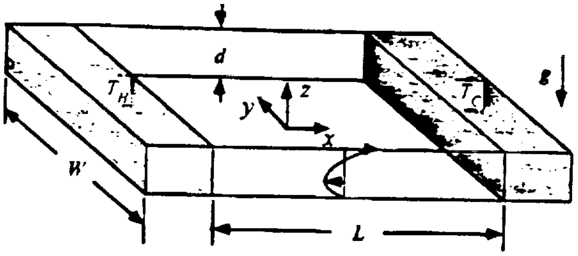

FIGURE 1. Problem geometry and coordinate specification.

at the top and cooling at the bottom to provide a stable axial-buoyancy gradient. The free surface of the liquid bridge is thus subject to a temperature gradient and the flow in the bulk is driven by the resulting thermocapillary convection.

The first documentation of oscillatory thermocapillary convection in half-zones is due to Schwabe *et al.* (1978) and Chun & Wuest (1979). Both groups measured the oscillating temperature fields in half zones with diameters of a few millimetres and found oscillations with frequencies of the order of 1 Hz. More in-depth experimental studies of oscillatory flow in half-zones can be found in the work of Preisser, Schwabe & Scharmann (1983) and Velten, Schwabe & Scharmann (1991). Recent theoretical work on the half-zone problem has been performed by Shen *et al.* (1990), Neitzel *et al.* (1991, 1993), Wanschura *et al.* (1995) and Levenstam & Amberg (1995). The first two of these studies employ energy-stability theory, the next pair, linear-stability theory, and the final one, direct numerical simulation of a model half-zone problem. The results of the various theoretical approaches are in agreement with each other and in reasonable agreement with available experimental results (see e.g. Velten *et al.* 1991)) on half-zones.

Au: not in Ref.

added on p. 21

The flow examined in this work is that of a thin liquid layer of depth d in a horizontal, rectangular slot driven by both thermocapillary and buoyancy forces as shown in figure 1. This flow possesses some of the central features of the half zone such as a return-flow basic state, a velocity profile for which is sketched in the figure. The geometry allows for very large aspect ratios L/d and W'/d to minimize the effects of endwalls and sidewalls, respectively. By changing the depth of the layer, control over the influence of buoyancy is also possible. A temperature gradient is produced on the free surface by maintaining a temperature difference $\Delta T = T_H - T_c > 0$ between the two endwalls; the sidewalls and bottom are assumed adiabatic. Since $\gamma > 0$, the thermocapillary stress pulls the free surface from the hot wall to the cold wall. Buoyancy also serves to drive the flow in the same direction as thermocapillary forces, but the case of greatest interest in this study is that for which thermocapillary effects are dominant, implying thin liquid layers.

The strength of thermocapillary convection is characterized by the Marangoni number,

$$Ma_L = \frac{\gamma d^2 \Delta T}{\mu \alpha L}, \tag{1}$$

where μ is the dynamic viscosity, α is the thermal diffusivity, and L is the streamwise domain length indicated in figure 1. This definition facilitates the comparison of experimental results from different length slots, since the driving force for the flow is $\Delta T/L$; however, it differs from that used in theoretical treatments for layers of infinite horizontal extent, i.e.

$$Ma = \frac{\gamma d^2\, \partial T/\partial x}{\mu\alpha}, \tag{2}$$

which employs the temperature gradient along the interface. We shall refer to the quantity defined in (1) as the *laboratory* Marangoni number, and indicate it by the L subscript. Owing to the existence of thermal boundary layers near both the hot and cold walls, $Ma_L > Ma$, where the value of $\partial T/\partial x$ employed in (2) is that in the interior, 'core' region, of the flow, where the surface-temperature variation is nearly linear. The definition of Ma provided in (2) permits easier comparison with available theory for infinite layers, but requires an *a posteriori* measurement of $\partial T/\partial x$. If one believes that the instability of this core flow is responsible for observed oscillations in very thin layers and that end effects serve merely to modify these, then Ma is the true Marangoni number of interest since it is apparatus-independent. As layer depth d decreases for fixed L (see figure 1), the core region of the flow exhibits a more nearly linear variation of surface temperature with streamwise distance. Consequently, as $d/L \rightarrow 0$, we expect better agreement between experiment and theory due to the existence of a more linear thermal field and also to the reduced effect of the endwalls on the core velocity field.

Buoyancy effects can be quantified in terms of the dynamic Bond number,

$$Bo_D = \frac{\rho g \beta d^2}{\gamma}, \tag{3}$$

which is a measure of the relative strength of buoyancy forces to thermocapillary forces. Here ρ is the density, g is the gravitational acceleration, and β is the thermal-expansion coefficient. The dynamic Bond number can be formed as Ra/Ma, where Ra is a Rayleigh number which uses the same horizontal ΔT as the Marangoni number.

Also of importance in these flows is the Prandtl number, $Pr = \nu/\alpha$, where ν is the kinematic viscosity. The Prandtl number for the liquid used in this study is $O(10)$, which implies a strong coupling between the thermal and momentum fields. Either of the Marangoni numbers defined above may be expressed as the product of the Prandtl number and a corresponding Reynolds number, i.e. $Ma_L = Re_L Pr$ or $Ma = RePr$.

Since the thermocapillary-driven surface flow in the closed domain of figure 1 creates a pressure gradient to drive the return flow, the normal-stress boundary condition on the free surface requires a non-zero surface curvature (Davis & Homsy 1980). However, in the limit of infinite mean surface tension the surface becomes flat, and hence a constant-depth thermocapillary slot flow as sketched in figure 1 is possible. Two dimensionless groups that indicate the amount of surface deflection are the surface-tension number

$$S = \frac{\rho d \sigma}{\mu^2}, \tag{4}$$

and the capillary number,

$$Ca = \frac{\mu U}{\sigma}. \tag{5}$$

A flat free surface is achieved if $S \rightarrow \infty$, and $Ca \rightarrow 0$. In the present experiments, S and Ca are typically of the order of 25000 and 0.001, respectively, indicating that the assumption of a flat free surface is reasonable.

Pure thermocapillary convection and its counterpart including buoyancy have received attention from both theoreticians and experimentalists. Sen & Davis (1982) computed states of steady two-dimensional thermocapillary flow in slots, including free surface deformation. Smith & Davis (1983) investigated the stability of a return-flow basic state in the core of such a slot to convective instabilities, finding a new form of instability which they termed a ***hydrothermal wave***. This mode is a temperature-disturbance wave that propagates in a direction which depends on the liquid's Prandtl number. For small Pr, the waves propagate transversely across the layer and for large Pr the direction is nearly opposite that of the surface flow. For intermediate Pr, the hydrothermal waves are predicted to propagate obliquely against the surface flow, and this behaviour is the expected one for the experiments presented in this paper. The physics of the instability mechanism were later elucidated by Smith (1986) for the small- and large-Pr limits in terms of the interaction between the thermal field and the inertially (low Pr) or viscously (high Pr) dominated flow field. For the Prandtl number (approximately 14) of the liquid used in these experiments, the high-Pr mechanism is the more relevant one. In this limit the hydrothermal-wave instability is sustained by the coupling between the convection of thermal disturbances by the basic-state velocity field, and conduction of these disturbances to create new instability-initiation spots. Extension of the Smith & Davis theory to account for the influence of buoyancy forces has been done by Garr-Peters (1992*a*, *b*), Parmentier, Regnier & Lebon (1993) and Mercier & Normand (1996).

Kirdyashkin (1984) was the first to analytically investigate combined thermocapillary–buoyancy-driven flow in a thin two-dimensional slot in the core region away from the endwalls. He presents both velocity and temperature profiles, and also includes experimental results obtained using ethyl alcohol in a 900 mm slot with a typical layer depth of 10–20 mm. Steady-state profiles are fully developed in the core region, agreeing well with analytical solutions. A parallel-flow core region is typically observed in the middle 90% of the domain, with endwall influence extending approximately three layer depths from each wall.

Villers & Platten (1992) conducted experiments and performed two-dimensional numerical simulations of combined thermocapillary–buoyancy flow in a thin layer of acetone ($Pr = 4.2$). A central finding of their work is that, as the Marangoni number increases, the flow transitions from a single steady convection cell, to multiple steady cells, and then to an oscillatory state with oscillation periods on the order of 5 s. De Saedeleer *et al.* (1996) have performed more recent experiments in decane ($Pr = 15$), observing also that the first transition is to a steady multicellular state. We shall see from the present results that a combination of buoyancy and geometric factors are likely to be responsible for this deviation from the Smith & Davis (1983) transition scenario.

9

Schwabe *et al.* (1992) have documented similar behaviour in slot and annular-pan geometries employing layer depths of ethanol ($Pr = 17$) on the order of a few millimetres. Here, multiple steady multicellular structures are also observed. Transition Marangoni numbers for the various regimes are determined; that from a single steady cell to multiple steady cells occurs for $Ma > 600$, and the transition from multiple steady cells to an oscillatory state is observed for $Ma > 3000$. Most of the reported results are for the annular-pan geometry, for which no theoretical results are presently available. Schwabe *et al.* (1992) report two different types of oscillatory flow states, depending on the layer depth: for $d < 1.4$ mm, a short-wavelength azimuthally travelling state is seen, while, for $d > 1.4$ mm, a long-wavelength state with a radially propagating component is observed. Results of the present work could imply that the difference between these two states may be related to an effect of the dynamic Bond number. Unfortunately, very few results are reported for the rectangular geometry, which is very similar to that employed for the present experiments. Those which are provided are for the single layer depth of 1.8 mm, which is likely to be too deep to observe pure hydrothermal waves, as will be noted later.

The primary aim of the experiments described in this work is to examine combined thermocapillary–buoyancy convection in thin horizontal layers, with the goal of observing a pure hydrothermal-wave instability. This has been successfully accomplished. Since this instability is believed to be responsible for the degradation of material grown via the float-zone process, the possibility of eliminating such oscillations is of interest. In Part 2 (Benz *et al.* 1998), the feasibility of suppressing hydrothermal waves through active periodic heating of lines on the free surface is demonstrated for the moderate-Pr liquid used in these experiments. However, it must be emphasized that the hydrothermal-wave instabilities which occur in a liquid of moderate Prandtl number are driven by a different mechanism (Smith 1986) from that responsible for similar instabilities in low-Prandtl-number liquids characteristic of liquid metals.

2. Experimental setup and techniques

2.1. *Working liquid and apparatus*

The working fluid used in these experiments is 1 cS Dow Corning silicone oil. It has the desirable properties that it is transparent to visible light, allowing both flow visualization and quantitative measurement using laser-Doppler velocimetry (LDV), and has a free surface which is relatively resistant to contamination. In addition, we shall examine the spanwise structure of the observed instabilities by visualizing the thermal field of the free surface using an infrared camera. The chosen oil also has an absorption band in the infrared within the detectable wavelength range of this camera which is strong enough to allow infrared visualization of the liquid's surface temperature rather than that in the bulk.

The Prandtl number of the silicone oil used here is $Pr = 13.9$, indicating that the thermal field is strongly coupled to the velocity field and, according to the theory of Smith & Davis (1983), the preferred instability should be a hydrothermal wave. The properties of the oil, coupled with the thin layers investigated here ($O(1$ mm$)$), also ensure that the free surface of the layer is flat. A fluid possessing a low vapour pressure is also desirable in thermocapillary flow experiments due to the likelihood of evaporation at the hot end of the apparatus. The 1 cS oil was chosen after experimenting with silicone oils with viscosities in the range of 0.65–10 cS in part because it was found to have the fewest problems with evaporation.

The test cell was designed with the goal of observing a hydrothermal-wave instability: a schematic of the cell is shown in figure 2. The length L and width W of the flow section are 30 mm and 50 mm, respectively; for the range of layer depths examined in this work, these choices afford streamwise (x-direction) and spanwise (y-direction) aspect ratios of $12 \leqslant L/d \leqslant 40$ and $20 \leqslant W/d \leqslant 67$, respectively. These permit both the establishment of a well-developed return-flow velocity profile in the core region away from the walls and the accommodation of a relatively large number of hydrothermal waves. For a liquid with $Pr = 13.9$, the linear-stability analysis of Smith & Davis (1983) predicts a most-dangerous disturbance with a wavelength of approximately $2.4d$, propagating upstream at an angle of 20° to the streamwise direction of the basic state. Thus, at least a dozen hydrothermal waves can exist in the domain, and the large spanwise extent of the apparatus allows minimized impedance in the oblique propagation direction.

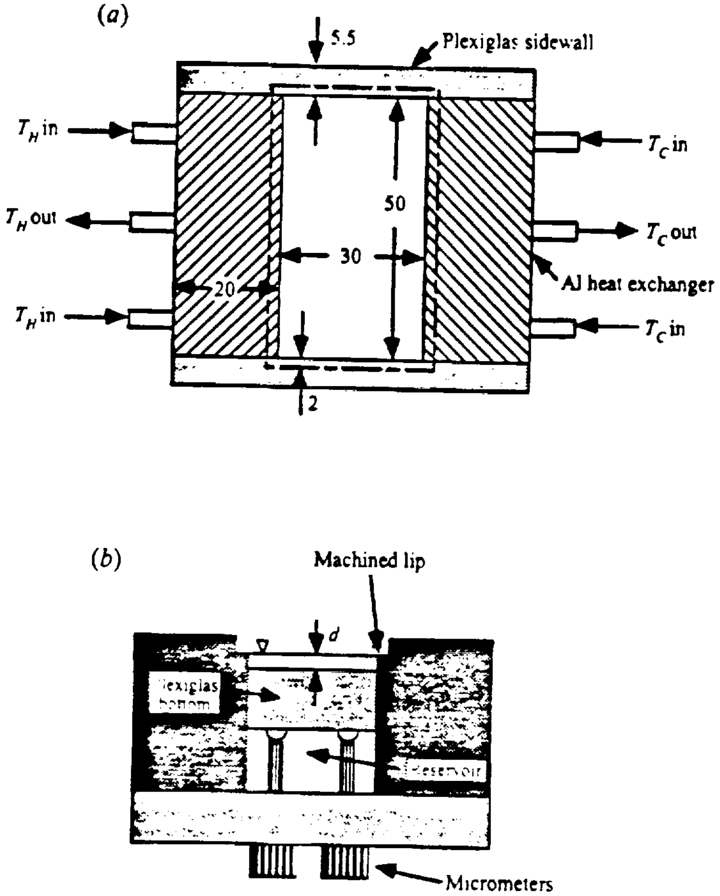

t/ovr

FIGURE 2 Experimental apparatus schematic (all dimensions are in mm): (a) top view; (b) side view.

To provide an accurate determination of the depth d and its continuous variability, the apparatus was designed with a movable base and reservoir, as seen in the side view of figure 2(b). The base is a machined Plexiglas block which fits snugly within the cavity created by the endwalls and sidewalls, yet has very small gaps ($O(0.025$ mm$)$) between it and the vertical walls which permit the addition of liquid to the layer through the reservoir. Three ball bearings mounted in the underside of the base ride on micrometers, allowing depth adjustment of the flow domain to within 0.005 mm. The apparatus is filled by injecting silicone oil into the reservoir, as suggested above. The sidewalls are also constructed of Plexiglas in order to approximate adiabatic boundary conditions. The endwalls, through which temperature-controlled water is circulated, are aluminium to provide uniform constant-temperature boundary conditions at both endwalls. Endwall temperatures are measured directly using thermocouples mounted in the centre of each endwall a distance of 1 mm from the surface which is in contact with the oil. The difference in endwall temperatures is able to be resolved to within 0.05 °C.

In order to achieve a definite and repeatable layer depth without a meniscus, a 90°, 2 mm lip has been machined along the top of the sidewalls and endwalls which serves to pin the contact line of the silicone oil. The upper surface of this lip is coated with a fluorad (3M Scotchguard) surface-modifying treatment, which inhibits the liquid from wetting the lip. The existence of this lip with a pinned contact line is crucial to the establishment of a layer of uniform depth. Levelling of the apparatus is achieved by mounting it on a three-point micrometer-type tilt table. Adjustments to the tilt are made while observing the reflections of a grid in the free surface near the lip regions, and continue until the grid appears undistorted at all points along the lip, indicating a flat free surface. Isolation from laboratory vibrations is achieved by securing the tilt table to a commercial vibration–isolation table.

Two approaches were investigated for minimizing disturbances at the free surface due to transient laboratory air currents. The first was to cover the apparatus with a Plexiglas lid allowing a 5 mm thick gas layer above the free surface. However, this method experienced problems with condensation of trapped silicone-oil vapour at the cold wall. The formation of droplets on the cold horizontal lip ultimately results in the loss of the pinned contact line, requiring the cessation of experiments and the cleaning and re-coating of the apparatus. An alternative technique was successful, however. A Plexiglas shroud 60 mm × 60 mm in cross-section and 100 mm in height was placed around the flow cell. Since the upper end of the shroud was open to the laboratory, over time liquid depletion due to evaporation results in a change in the position of the free surface. Although the rate of evaporation is quite small ($O(0.1\ \mu\mathrm{l/s})$), the resulting depth change is unacceptable for these experiments. Hence, the evaporating silicone oil was replaced by liquid supplied from a constant-head container to the reservoir at the required rate. At the typical re-supply rate, the effective vertical velocity at the free surface is roughly $0.07\ \mu\mathrm{m\ s^{-1}}$ or about 0.001% of the measured free-surface speed, and is therefore felt to have a negligible impact.

Properties of the Dow Corning 200, 1 cS silicone oil used in these experiments were obtained from the manufacturer, with the exception of the surface tension. These data were measured directly by colleagues at the Microgravity Advanced Research Support (MARS) Center in Naples, Italy using the wire loop method for the range of the temperatures encountered in the present experiments. From these measurements, a linear least-squares fit of the data yielded the result

$$\sigma(T) = 17.237 - 0.0755(T - T_0)\ \mathrm{mN\ m^{-1}} \qquad (6)$$

where $T_0 = 25$ °C was the reference temperature about which experiments were performed.

2.2. *Experimental techniques*

Four different experimental techniques were used to explore the flow states encountered in this work. Quantitative measurements of steady-state velocity fields, both prior to and subsequent to the onset of instability, were performed with a TSI single-component LDV. The flow was seeded with dilute amounts of silicon-carbide particles with a mean diameter of 1.5 μm. Velocity-profile measurements through the depth (z) of the layer allow one to see the degree to which the assumed return-flow basic state is achieved; measurements as a function of streamwise (x) and spanwise (y) distance permit an assessment of the influences of endwalls and sidewalls, respectively.

Flow visualization experiments were performed using two techniques. For the first, the flow was seeded with polystyrene microspheres with diameters ranging from 1–15 μm and these were observed within a 1 mm thick laser-sheet illumination of an (x, z)-plane. A Dage-MTI CCD camera was used to record the resulting images for both steady and unsteady flow conditions. Since the particles were slightly more dense than the test liquid, problems were experienced with keeping the particles from settling to the bottom. In a static fluid, particle settling time through the depth of the layer (at 10 μm s^{-1} for an average 8 μm particle) is roughly two minutes; for dynamic experiments, particles remain in suspension longer, but insufficiently long for the method to be useful for extended periods of time. The second technique employed was shadowgraphic visualization across (i.e. in the *y*-direction) the layer. Thermally induced index-of-refraction variations, integrated through the span of the layer, were likewise recorded using the CCD camera. While no attempt was made to extract quantitative data from these results, the shadowgraphic technique is quite sensitive, providing clear indications of both the existence of multicellular structures and unsteadiness. It is the visualization method of choice for pinpointing the flow transitions to be reported in §3. The only limitation of the technique, with regard to the present experiments, is the fact that the mean temperature gradient bends the light downward on its way to the camera so that, at some limiting depth, it is no longer possible to obtain clean shadowgraphic images of the flow. For this apparatus and the conditions of these experiments, this limiting depth is 0.75 mm.

The final technique used in these experiments was infrared thermography of the free surface. The use of this technique was central to the investigation of oblique hydrothermal-wave instabilities and to the suppression of these waves reported in Part 2. In addition, it permits the observation of the structure of the multicellular instability and its subsequent transition to oscillatory flow. These measurements were performed using an Amber AE-4128 infrared camera employing a 128 × 128 element indium-antimonide focal-plane-array detector, which is sensitive to radiation in the range of 1–5.5 μm. The output from the camera was captured with a variable-scan frame grabber mounted in an IBM-compatible 386 computer, allowing it to be displayed on a video monitor or recorded onto video tape. Further details on this and all other techniques employed in these experiments may be found in Riley (1995).

3. Results

The combination of methods described above was used to investigate the flow structures observable in the test cell over a range of conditions which was as large as possible, given the inevitable constraints imposed by the apparatus, test liquid and measurement techniques, some of which are described above. The results to be presented here will focus on the return-flow basic state, its instability to both hydrothermal waves and to a steady multicellular state, and the onset of time-dependent flow from the steady multicellular state. The transition map for the states observed is presented in terms of the laboratory Marangoni number Ma_L (equation (1)), and true Marangoni number Ma (equation (2)) in figure 3.

There are three major categories into which the observations fall: steady, unicellular flow (SUF); steady multicellular flow (SMC); and oscillatory flow. The last of these categories, however, may be further divided depending on whether the state preceding the onset of oscillatory flow was unicellular (leading to the hydrothermal waves (HTW) predicted by Smith & Davis 1983) or multicellular (leading to oscillating multicellular flow (OMC)). It should be pointed out that, while we have chosen to characterize the transitional Marangoni numbers in terms of the dynamic Bond number, there is the additional possible dependence of the transition sequence on the two aspect ratios L/d and W/d. Since this apparatus does not allow these to be held constant as the depth of the layer is varied, it is not possible to unequivocally attribute the observed transition to multicellular flow to a particular effect.

As noted in §1, Ma_L exceeds Ma, owing to the existence of thermal boundary

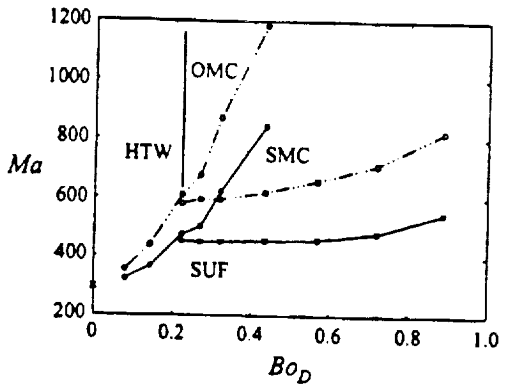

FIGURE 3. Transition map of the experimental results in terms of Ma_L (open symbols) and Ma (closed symbols) for transitions to hydrothermal waves (HTW), steady multicells (SMC) and oscillating multicells (OMC). The single × plotted on the ordinate corresponds to the linear-theory result of Smith & Davis (1983) for the onset of hydrothermal waves.

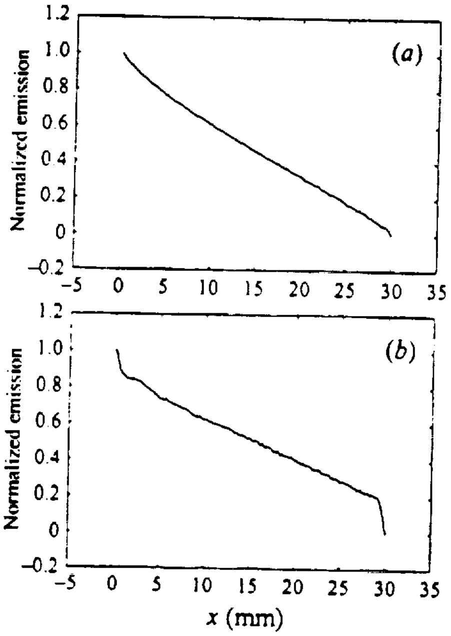

FIGURE 4. Normalized IR camera emission for the steady unicellular state (just prior to onset) along the streamwise coordinate in the centre of the span for a layer of (*a*) 0.75 mm thickness; and (*b*) 2.5 mm thickness.

layers at the temperature-controlled endwalls, particularly for moderate-to-high-Pr liquids such as the one employed here. These boundary-layer effects become more pronounced as the layer depth increases, as seen in figure 4, which shows a normalized emission from the IR camera along a line in the middle of the span of the layer as a function of streamwise distance x for two different layer depths. For both cases in figure 4, the emission profiles correspond to a state of steady unicellular flow just prior to the appearance of either hydrothermal waves (figure 4*a*) or steady multicellular flow (figure 4*b*).

In order to correct the Marangoni number for this effect, the emission data in

d (mm)	Bo_D	Ma_L (HTW)	Ma (HTW)	Ma_L (SMC)	Ma (SMC)	Ma_L (OMC)	Ma (OMC)
0.75	0.080	355	324	n.o.	n.o.	n.o.	n.o.
1.00	0.142	440	366	n.o.	n.o.	n.o.	n.o.
1.25	0.222	609*	~~366~~ 476*	580	453	n.o.	n.o.
1.375	0.269	n.o.	n.o.	595	451	677	503
1.50	0.320	n.o.	n.o.	595	452	871	621
1.75	0.435	n.o.	n.o.	619	455	1185	842
2.00	0.569	n.o.	n.o.	658	459	n.i.	n.i.
2.25	0.720	n.o.	n.o.	711	482	n.i.	n.i.
2.50	0.889	n.o.	n.o.	822	547	n.i.	n.i.

TABLE 1. Transitional Marangoni numbers versus depth and dynamic Bond number for transitions to hydrothermal waves (HTW), steady multicells (SMC) and oscillating multicells (OMC). The asterisks mark a case which is not a true transition to HTW, n.o. denotes not observed, and n.i. not investigated.

the interior region of the flow, i.e. $5 \leqslant x \leqslant 25$ mm, are fit with a straight line, which, along with the calibration data (including the known measured temperatures of the endwalls), is used to extract $\partial T/\partial x$ for the core region. This same procedure is employed for determining the core temperature gradient used to correct the transition map for the steady → oscillatory multicellular regime as well, although the data in this case are of the type seen in figure ~~9~~10(a). In all cases, the temperature gradient is determined for a state just prior to the onset of the transitional state. De Saedeleer *et al.* (1996) also recognized the importance of determining the core temperature gradient, which they did using a thermocouple inserted below the free surface.

? Au
10
Yes

One advantage to the present method for determining the true temperature gradient $\partial T/\partial x$ occurring in the core of the layer is that there is no need to determine the effective emissivity of the liquid or to calibrate the grey-level values against a blackbody emission source. By taking the ratio of the linear fit to the grey-level data in the core to the gradient represented by the maximum and minimum grey levels occurring at the endwalls of the same data, the absolute values of the free-surface temperature need not be determined.

Since the determination of Ma requires an *a posteriori* measurement of the core surface-temperature distribution, this was not necessarily done for cases not associated with transitions between states. Rather, the more convenient laboratory Marangoni number Ma_L is reported in the following sections when comparing to specific experimental cases. The transitional values of both Marangoni numbers are reported as a function of both the dimensional depth and dimensionless Bo_D in figure 3 and table 1. #

3.1. *Steady unicellular flow*

Of interest in characterizing this state is determining the degree to which the apparatus utilized for these experiments permits the establishment, in the core region away from vertical boundaries, of the return-flow basic state assumed in the theoretical analysis of Smith & Davis (1983). To this end, detailed LDV measurements have been performed for two states. The first case, with $(Ma_L, Bo_D) = (350, 0.142)$ corresponds to a layer of 1.0 mm depth at a Marangoni number which is ~~77~~% of the value at which transition to the hydrothermal-wave state was observed. The second case, with $(Ma_L, Bo_D) = (475, 0.320)$, is for a 1.5 mm layer depth, which first experiences a 80%

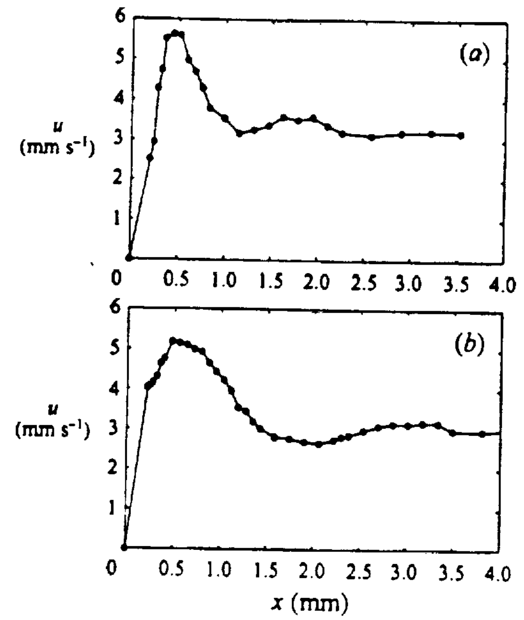

FIGURE 5. Horizontal 'surface' velocity near the hot wall: (*a*) $d = 1.0$ mm; (*b*) $d = 1.5$ mm.

transition to steady multicellular flow. The chosen Marangoni number is the same fraction (~~7~~%) of the transition value to the new state as for the first case.

37%

figures 5 and 6 show the variation of the x-component of 'surface' velocity near the hot and cold walls, respectively, for the two cases. These measurements were performed with the LDV fiber-optic head oriented above the layer, looking downward. It is estimated (Riley 1995) that the centre of the measurement volume (an ellipsoid with a major axis of 120 μm) is roughly 60 μm below the free surface. Measurements for both hot walls show an overshoot of the core velocity followed by an equilibration which takes place within a distance $x/d = 3$ in both cases. At the cold walls, no such overshoot is observed and the effect of the endwall is constrained to a region of approximately $x/d = 2/3$ in length.

caps F

It is possible that the observed overshoot and recovery at the hot wall are due to the formation of a strong roll cell there, in some sense a precursor to the steady multicellular state to be discussed in §3.3. Such a cell was observed even for low-Bo_D cases at Marangoni numbers immediately preceding the transition to hydrothermal-wave instability. The overshoot in velocity is consistent with LDV measurements and calculations performed by Villers & Platten (1992) for flows of acetone ($Pr = 4.24$) in containers of modest aspect ratio.

Another numerical study which has relevance to the endwall region velocity measurements is that of Ben Hadid & Roux (1990), who performed numerical calculations of thermocapillary convection in a long horizontal layer for a low-Prandtl-number fluid. Since Pr is assumed to be small, the momentum and thermal fields are decoupled, and the case of a constant applied shear stress at the free surface was considered. Thus, there are significant differences between this work and the high-Pr situation considered presently. One of the cases computed by Ben Hadid & Roux has an aspect ratio $L/d = 25$, which is comparable to the present 1 mm and 1.5 mm layers which have $L/d = 30$ and 20, respectively. For the lowest-Reynolds-number case ($Re = 66.7$) presented by Ben Hadid & Roux, the free-surface velocity increases

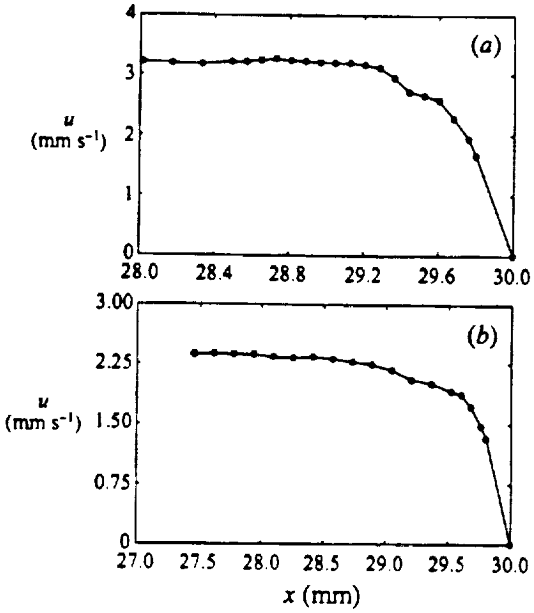

FIGURE 6. Horizontal 'surface' velocity near the cold wall: (*a*) $d = 1.0$ mm; (*b*) $d = 1.5$ mm.

monotonically away from the hot wall and decreases in a similar fashion near the cold wall, exhibiting no overshoot at either end of the slot, contrary to what has been observed in the present experiments, although this is expected in light of the free-surface conditions assumed in the calculations. The two experimental cases under discussion correspond to Reynolds numbers of $Re = 23.4$ and 34.1, respectively, for the 1.0 mm and 1.5 mm layer depths.

Measurements of surface velocity (similar to those of figures 5 and 6) made in the vicinity of the adiabatic sidewalls indicate that the free-surface velocity reaches its core value much more rapidly than observed near the heated endwalls (Riley 1995). For the cases examined, this adjustment at the streamwise centre of the layer takes place within a single layer depth.

In the core region, away from both endwalls and sidewalls, LDV measurements made through the layer indicate the degree to which the return-flow basic state is attained. The quadratic profile of Smith & Davis (1983) is modified by the existence of buoyancy. Solution of the two-dimensional Boussinesq equations for fully developed flow in the core yields the horizontal velocity,

$$U(z) = \tfrac{3}{4}z^2 - \tfrac{1}{2}z + Bo_D\left(-\tfrac{1}{6}z^3 + \tfrac{5}{16}z^2 - \tfrac{1}{8}z\right), \tag{7}$$

where length has been scaled by the depth d and velocity by the thermocapillary velocity

$$U_s = \frac{\gamma(\partial T/\partial x)d}{\mu}. \tag{8}$$

Figure 7 shows measured and theoretical profiles of $U(z)$ for the two layers considered in this section. Measurements were performed by having the two intersecting beams of the LDV enter the flow field through one of the adiabatic sidewalls. This orients the major axis of the ellipsoidal measurement volume normal to the z-direction in which the largest velocity gradients occur. Velocity-gradient broadening is there-

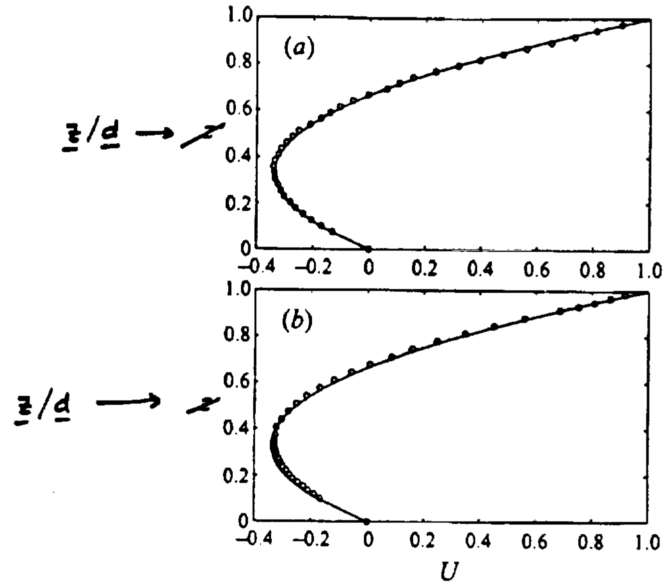

FIGURE 7. Basic-state velocity profiles for: (*a*) $d = 1.0$ mm, $Ma = 350$; open circles, LDV measurements; solid line, theory for $Bo_D = 0$; (*b*) $d = 1.5$ mm, $Ma = 475$; open circles, LDV measurements; solid line, theory for $Bo_D = 0.32$.

fore confined to the 40 μm waist dimension of the measurement volume. In order to obtain data near the bottom (free surface) of the layer, the plane of the beams entering through the sidewall is angled slightly downward (upward) to position the measurement volume as close as practicable to the location of interest. Near the free surface, where the uncertainty in the measurement is largest, the size of the standard deviation in the dimensional velocity for the 1.0 mm layer of figure 7(*a*) is $O(0.2\ \mathrm{mm\ s^{-1}})$, compared with a maximum measured speed of roughly 4 mm $\mathrm{s^{-1}}$. In the cases shown in figure 7, the velocity has been scaled by its maximum value at the free surface, as opposed to the thermocapillary velocity scale. For the thinner layer, the comparison between the measurements and theory is made for $Bo_D = 0$, indicating the degree to which this layer conforms to the theoretically assumed basic state of Smith & Davis (1983). In both cases, the comparison between measured data and theoretical profiles is excellent.

One final question regarding the unicellular state observed in these experiments is the degree to which flow in the core region is independent of the x-direction of figure 1. In order to assess this, measurements of the maximum value of the interior (backflow) velocity were performed at several locations between the two heated endwalls, as shown in figure 8. The points displayed as circles are all scaled using a constant value of U_s (equation (8)) corresponding to the conditions at the rightmost cold point, where the properties are computed using a conduction solution for the temperature. These data indicate the existence of a fair amount of variation between the endwalls. Speculating that a large part of this variation may be due to the temperature dependence of viscosity, we have adjusted the velocities depending on the local value of U_s, computed using the same conduction solution for temperature. The adjusted values, shown in figure 8 as squares, show much less variation, lending some credence to the hypothesis.

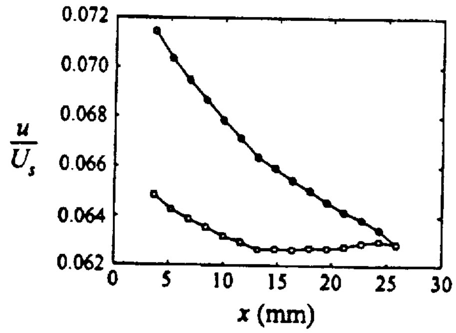

FIGURE 8. Maximum measured backflow velocity versus streamwise distance: circles, scaled by a constant U_s; squares, scaled by $U_s[T(x)]$, where T is obtained from a conduction solution.

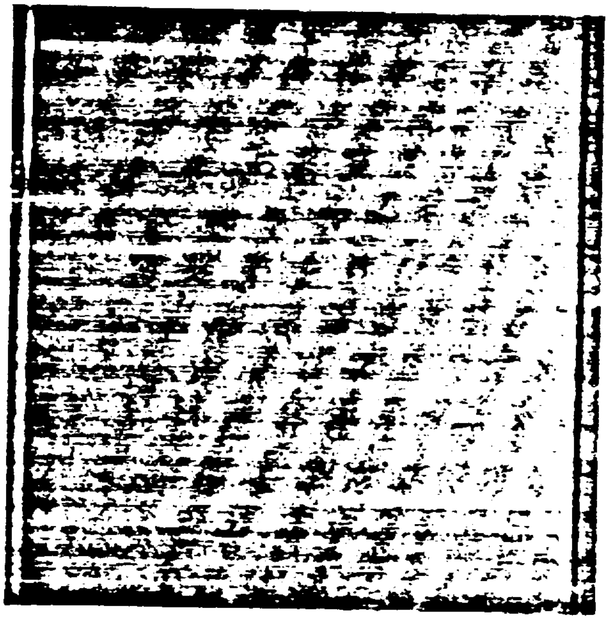

FIGURE 9. Instantaneous thermograph of hydrothermal waves on a 1.0 mm deep layer, viewed from above. The hot and cold walls are at the left- and right-hand sides of the figure, respectively, and the hydrothermal waves are propagating from lower-right to upper-left.

3.2. *Hydrothermal waves*

The state of greatest interest in the present experiments is that which results from instability of the unicellular basic state at low values of the dynamic Bond number. These hydrothermal waves are travelling thermal waves which, for the Prandtl number of the liquid used in these experiments, propagate obliquely, with a component which opposes the direction of free-surface motion. For $Pr = 14$ and $Bo_D = 0$, the theory of Smith & Davis (1983) predicts a wavelength of approximately $2.5d$ and a propagation angle $\Psi \approx 20°$ with respect to the negative x-direction. In these experiments, the hydrothermal-wave transition is observed for $Bo_D \leqslant 0.22$, corresponding to layer depths $d \leqslant 1.25$ mm.

The onset of time-dependence in this case is an especially sharp one to which the shadowgraphic visualization technique is particularly sensitive. The qualitative stucture of the flow, when viewed from above with infrared thermography is clearly

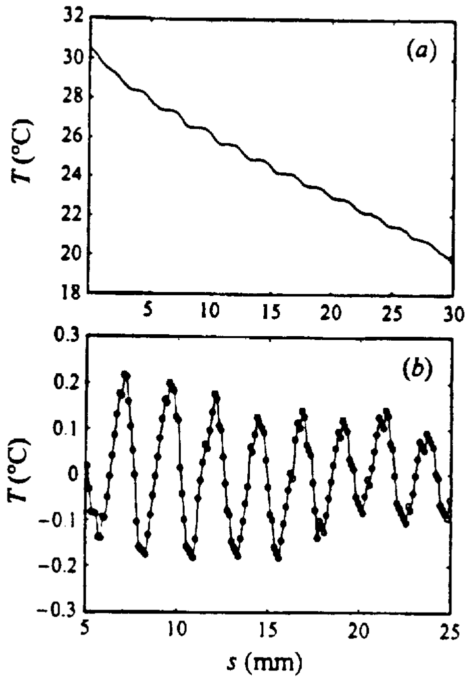

FIGURE 10. Instantaneous total temperature (*a*) and deviation from the local mean (*b*) along a line perpendicular to hydrothermal wave fronts.

in agreement with that predicted by Smith & Davis (1983). This is shown in figure 9 for a layer of 1.0 mm depth at a condition which is slightly supercritical. In accordance with the nonlinear theory of Smith (1988), only one of the two possible families of hydrothermal waves is observed. If the apparatus is level and the base and free surface are parallel (which is essential to the attainment of this state), either of these families may appear. It is clear from this thermograph that the hydrothermal waves completely fill the domain with little influence from the endwall boundaries. The same is true of the sidewall boundaries, as well, although not observable in this figure; they are constructed from Plexiglas, and hence behave as nearly adiabatic boundaries. Although very difficult to observe in figure 9, there does exist a single steady roll cell located at (and parallel to) the hot wall toward which the hydrothermal waves propagate. This cell is consistent with its appearance even in the states which have been termed unicellular. It is also apparent from the figure that the wavelength increases slightly as the waves propagate across the layer from the cold wall to the hot one. This could be a ramification of the fact that the core flow is changing with x due to the temperature dependence of viscosity, as discussed earlier, or the fact that the wavelength depends on the Prandtl number, which also varies locally with the temperature.

The temperature perturbations associated with these hydrothermal waves may be obtained from the infrared camera data. Figure 10 shows both the temperature variation (figure 10*a*) and perturbations (figure 10*b*) obtained by subtracting the mean-temperature variation along a line perpendicular to the wave fronts for data extracted from the thermograph of figure 9. From these data, it is seen that the amplitude of the temperature perturbation is not constant, but increases in the direction of propagation from roughly 0.2 °C to 0.35 °C peak-to-peak.

d (mm)	λ (mm)	f (Hz)	c (mm s^{-1})	Ψ (deg.)
0.75	1.95	0.98	1.91	27.9
1.00	2.58	0.57	1.47	23.2
0.25	3.37	0.38	1.28	22.4

t/o

TABLE 2. Dimensional wavelength, frequency, phase speed and propagation angle as a function of layer depth for hydrothermal-wave cases.

Bo_D	λ/d	fd/U_s	c/U_s
0.080	2.60	0.0236	0.0614
0.142	2.58	0.0217	0.0561
0.222	2.70	0.0174	0.0469

t/o

TABLE 3. Scaled wavelength, frequency and phase speed as a function of dynamic Bond number for hydrothermal-wave cases.

The structure of the hydrothermal-wave instability is quantified in terms of wavelength λ, frequency f, wave speed c, and angle of propagation Ψ for the three cases examined in this work. All of the quantities were extracted from the infrared images of the free-surface temperature fields at values of ΔT slightly above critical. Dimensional values of these quantities are presented in table 2; dimensionless values of λ, f and c are given in table 3, where wavelength has been scaled by depth, wave speed by the thermocapillary velocity scale U_s (equation (8)) and frequency by U_s/d. The dimensionless wavelength is seen to be comparable to the value $\lambda/d = 2.4$ predicted by the linear-theory zero-gravity analysis of Smith & Davis (1983) and is nearly independent of the depth of the layer. The variation of the other quantities with Bo_D is more substantial, so that comparison with a zero-gravity theory is less appropriate. A linear-stability analysis incorporating buoyancy has been performed for the Smith & Davis problem (Riley & Neitzel 1998) and a comparison of these results with the present experimental ones is discussed in detail there. Suffice it to say here that the linear-theory critical Marangoni number, Ma_C (plotted as the symbol × in figure 3), agrees almost exactly with Ma_L for the smallest value of Bo_D measured in these experiments, and that the trend in Ma_C with increasing Bo_D is the same for both theory and experiment.

Previous researchers have measured oscillations in thin thermocapillary-driven liquid layers, but have not provided conclusive evidence of the hydrothermal-wave instability. The experiments of Villers & Platten (1992) in a thin acetone layer ($Pr = 4$) utilize one-point LDV measurements to determine whether the flow at a single point in the layer was steady or oscillatory. In this manner they map out a boundary in (Ma, Ra)-space denoting the steady/oscillatory ~~boundary~~. No discussion on the structure of the flow producing the oscillations is given, since their measurements do not provide that type of information. Much of their data are for relatively thick layers ($d \geqslant 2.0$ mm, $Bo_D \geqslant 0.362$), and hence the observed oscillations are probably the oscillating multicellular flows to be discussed in §3.4, rather than hydrothermal waves. The study by De Saedeleer *et al.* (1996) reports the first instability in the form of a steady structure which then transitions to an oscillatory state. However, calculation of the Bond number associated with their experiments reveals that it is in excess of three times the maximum value determined for the first transition to a

transition/

hydrothermal-wave instability in the present experiments. In addition, their spanwise aspect ratio was quite small, which may have adverse effects for oblique waves.

Schwabe *et al.* (1992) discuss two different types of oscillatory thermocapillary flows in a thin annular geometry, so-called short- and long-wavelength instabilities. Their short-wavelength instability occurs in layers of $d \leqslant 1.4$ mm ($Bo_D \leqslant 0.18$), and has a wavelength of $\lambda \approx 6d$, for a 1 mm thick layer, whereas $\lambda = 2.58d$ for the 1 mm layer of the present study. The short-wavelength instability is investigated through single-point thermocouple measurements, and a shadowgraph technique that illuminates the oscillating meniscus formed at the lip of the inner wall of the annulus. The time variation of the meniscus at the lip appears wave-like, but no flow visualization in the bulk of the fluid is available. The dimensionless wave speed of the short-wavelength instability is $c = 0.06$ for a 1 mm thick layer, which is in agreement with the value of $c = 0.056$ for the 1 mm layer of the present study. Thus, it is possible that Schwabe *et al.* did indeed observe hydrothermal waves in an annular geometry, but the evidence is not completely conclusive on this point.

Ezersky *et al.* (1993) claim to have produced hydrothermal waves in 5 cS silicone-oil layers in the range of $1.2 \leqslant d \leqslant 3.1$ mm, but results are presented only for a 3.1 mm layer. The flow is investigated using a shadowgraphic technique, and an image is presented which is reportedly of a hydrothermal wave. For a layer depth of 3.1 mm, $Bo_D \approx 1.4$, which is much too large for the generation of pure hydrothermal waves according to the present results. Ezersky *et al.* present a shadowgraph image showing a disturbance with a wavelength of $\lambda/d \approx 1.3$, which is in the range of the steady multicellular flow structure discussed in the next subsection.

In a similar study, Daviaud & Vince (1993) report an observed travelling-wave disturbance in 0.65 cS silicone oil, for layer depths of $0.8 \leqslant d \leqslant 2.5$ mm. However, contrary to the results of the present study, the angle of propagation of the waves was found to be perpendicular to the applied temperature gradient ($\Psi = 90^\circ$). This could be due to the fact that their rectangular domain is quite large in the spanwise direction (200 mm), and relatively short in the streamwise direction (10 mm) in which the temperature gradient is applied. They also provide a graph of the critical applied-temperature difference (ΔT_{crit}) as a function of layer depth, which shows ΔT_{crit} decreasing with increasing depth for $0.8 \leqslant d \leqslant 1.4$ mm, followed by an increase for depths up to 2.5 mm. This behaviour is inconsistent with the results of the present study in which ΔT_{crit} decreases monotonically ($Ma_L \propto d^2$), and could be due to the difference in the geometries of the two flow domains.

3.3. *Steady multicellular flow*

The steady multicellular state observed at higher values of the dynamic Bond number are spanwise-uniform co-rotating rolls. Figure 11 shows the structure of this flow as observed by the three types of visualization techniques described in §2. In figure 11(*a*), a time exposure of sheet-illuminated particles clearly identifies the cellular structure and the associated saddle points in a layer of 2.0 mm depth; figure 11(*b*) shows an instantaneous snapshot of a combined shadowgraph/particle image; and figure 11(*c*) provides an overhead view of the temperature field visualized with infrared thermography. This last photograph clearly illustrates the two-dimensional nature of this flow state and the relative lack of influence of either sidewalls or endwalls.

Although it is impossible to ascertain from the thermographic image of figure 11(*c*), the strength of the cells decreases as one moves away from the hot wall. This may be observed by examining the streamwise variation of the horizontal velocity at a fixed vertical location, as shown in figure 12. This result is for a 1.5 mm

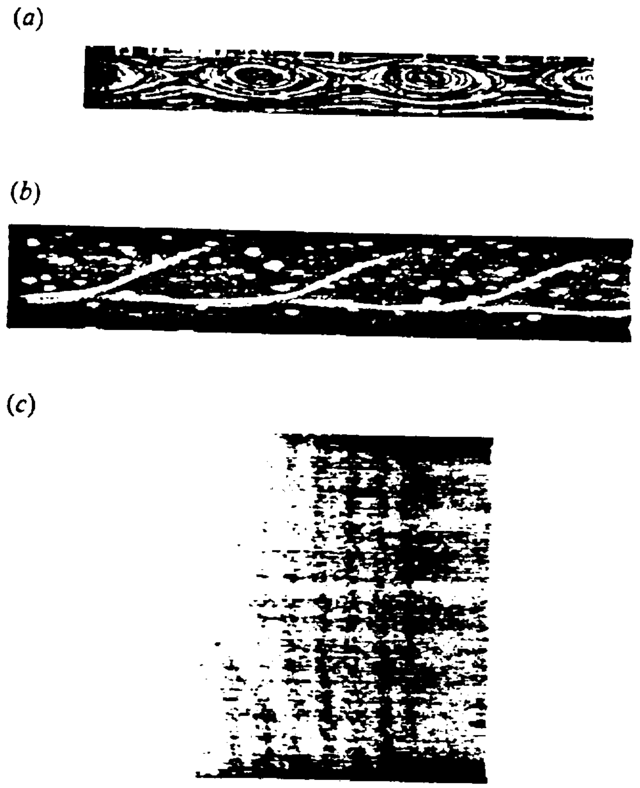

FIGURE 11. Steady, multicellular flow as visualized by: (*a*) particle-path time exposure for a 2.0 mm layer depth; (*b*) instantaneous shadowgraph with particles for a 1.5 mm layer depth; (*c*) thermograph for a 1.5 mm layer depth.

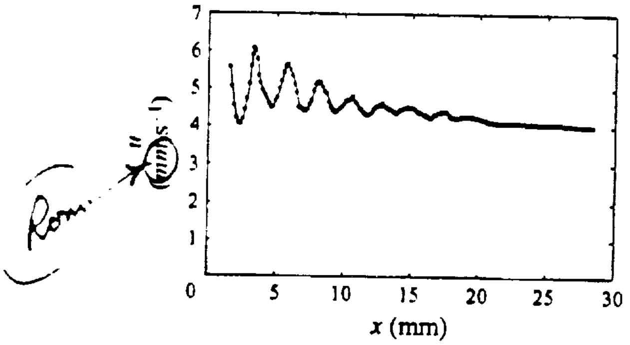

t/o

FIGURE 12 Horizontal velocity at $z/d = 0.9$ for steady multicellular flow in a 1.5 mm deep layer at $Ma = 800$.

7

layer depth at a value of $Ma_L = 800$, which is significantly higher than the steady multicellular-flow transition value of $Ma_L = 595$ for this Bo_D. Note that, even at this large temperature difference, the multicells decay rapidly in strength, vanishing at a distance of roughly $x/L = 2/3$. Also of note is the fact that the average velocity decreases when moving toward the cold wall, consistent with the earlier observation of a temperature-dependent viscosity effect.

The primary quantitative result to be obtained for this flow state, in addition

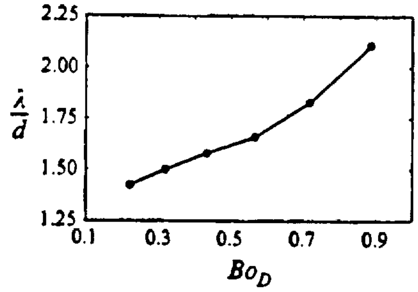

FIGURE 13. Dimensionless wavelength for steady multicellular states versus dynamic Bond number.

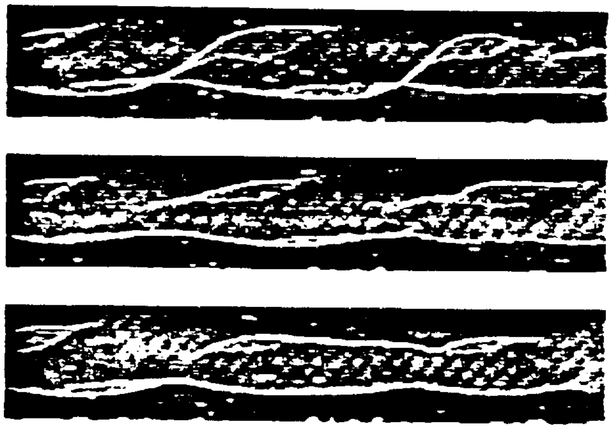

FIGURE 14 Instantaneous shadowgraphs at three instants of time (t is increasing from top to bottom) for the oscillatory multicellular state.

to the transition Marangoni number, is the dependence of the wavelength of the multicellular state on the dynamic Bond number. This is provided in figure 13, and exhibits relatively smooth, yet significant, variation. Once again, it is not possible to determine whether these observations are due to buoyancy or aspect-ratio effects. However, the degree of smoothness of the results indicates that the observed increase is certainly not due to abrupt quantum changes in the number of cells in the apparatus.

3.4. *Oscillating multicellular flow*

If the steady multicellular flow states of §3.3 are driven vigorously enough by increasing the Marangoni number, a second transition will take place to a~~n~~ time-dependent multicellular state. This state, although oscillatory, is not a pure travelling-wave state. This is evidenced by the sequence of shadowgraphs shown in figure 14, which shows the flow in a central portion of the apparatus. Time is increasing from top to bottom in the sequence, and the hot wall is to the left. Upon examining this sequence, there does not appear to be a well-defined wave speed associated with this state; there are pronounced differences between what is observed here and similar shadowgraphs for the pure hydrothermal-wave state of §3.2 (see Riley 1995). It is difficult to draw definite conclusions from such shadowgraph images, however, since the shadowgraph is integrated through the spanwise extent of the domain.

The free-surface thermograph shown in figure 15(*a*) provides greater insight into the structure of this flow. It is clear that there remain strong steady multicellular

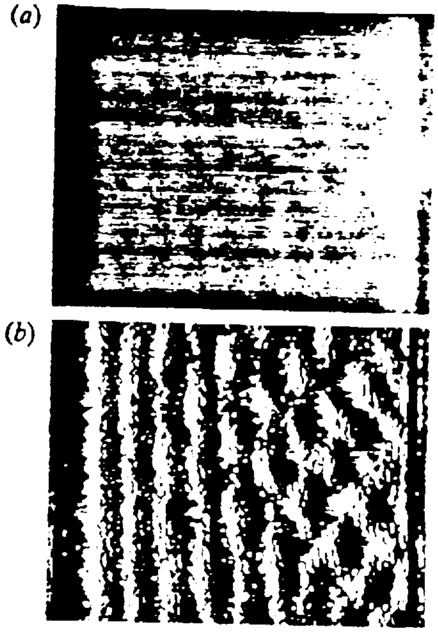

FIGURE 15. Instantaneous thermograph (*a*) and enhanced image (*b*) for the oscillatory multicellular state.

t/o

structures near the hot wall and a pair of oblique waves which appear to propagate through them, beginning at the cold wall. This is more evident in figure 15(*b*), in which data appearing in figure 15(*a*) have been enhanced through processing with an edge-finding filter, and subsequent binary windowing. A chevron pattern is observed near the cold wall which is suggestive of two interacting hydrothermal waves. In the absence of buoyancy, the nonlinear theory of Smith (1988) states that a single family should be observed (such as seen in figure 9) following instability of the pure return-flow basic state. However, the oscillatory instability observed here for large dynamic Bond numbers is reached from a different basic state (steady multicellular flow) than that considered by Smith, so his results are not strictly applicable. The image shows that the steady multicells are still established at the hot wall, despite the vigorous oscillatory convection on the cold-wall side of the domain.

An oscillatory multicellular state is also observed by Schwabe *et al.* (1992) in a rectangular domain, but the reported results for that apparatus are sparse. They note, however, that a 1.8 mm deep layer of ethyl alcohol experiences a transition from a unicellular flow to a steady multicellular flow, and subsequently to a time-dependent flow at $Ma_L = 3000$. Villers & Platten (1992) make no attempt to examine the structure of their oscillatory flow states in acetone, but for their layer thicknesses ($d > 2.0$ mm, typically), the results of the present study strongly suggest that they are actually observing oscillating multicellular flow.

4. Discussion

Experiments have been conducted to investigate the hydrothermal-wave instability of thermocapillary convection in a thin liquid layer first predicted by Smith & Davis (1983). The results of these experiments offer the first conclusive laboratory proof of the existence of this instability; results of previous experiments conducted in deeper layers have been clouded by the presence of buoyancy, geometric effects, or both. Present results for $Bo_D =$ ~~0.80~~ show a transition to oscillatory flow at a Marangoni number of $Ma = 324$, compared with the theoretical result (for a Prandtl number corresponding to the oil of these experiments) of $Ma = 295$ for $Bo_D = 0$; moreover, the results of figure 3 indicate that the experimental results asymptotically approach the theoretical limit as the Bond number decreases. The transition to hydrothermal waves from a state of steady unicellular flow (the core of which is shown to be an excellent approximation to the return-flow basic state of Smith & Davis), is a very sharp one. 0.080

In contrast, experiments performed with 'deep' layers do not experience a direct transition from the return-flow basic state to oscillatory flow, but rather first exhibit a steady multicellular structure. Whether this state is the result of instability due to buoyancy or due to finite-geometry effects (e.g. such as the imperfect bifurcation of Taylor–Couette → Taylor-vortex flow in finite annuli) is still uncertain. While even the smallest streamwise aspect ratio ($L/d = 12$) encountered in these experiments is comparatively large, since the present apparatus does not permit changing the depth of the liquid layer without also modifying the aspect ratio of the flow domain, these results alone are insufficient to answer this question. Recently, Cramer, Schneider & Schwabe (1997) have proposed a mechanism for the appearance of multicellular structures which involves the deceleration of flow on the free surface and the establishment of an accompanying bulk-pressure distribution which stimulates the formation of multiple cells. Certainly, near the ~~hot~~ wall, such a rapid deceleration does occur in the present experiments (as shown in figure ~~5~~), but then one might question why the thinner of the two layers shown in figure ~~5~~ (with the higher deceleration) first transitions to a hydrothermal-wave state, rather than to a steady multicellular state. Additional numerical and laboratory experimentation is necessary to completely answer this question. cold 6 6

Increasing the Marangoni number from a state of steady multicellular flow ultimately results in the transition to time-dependent flow. In appearance, this flow resembles a pair of obliquely propagating hydrothermal waves riding on top of the steady multicellular flow. Since the primary aim of the present experiments was the characterization (and suppression, in Part 2) of the hydrothermal-wave instability, attention was restricted in the case of the oscillating multicellular state to the determination of the transitional Marangoni numbers shown in figure 3 and listed in table 1.

The authors wish to acknowledge helpful discussions with Professors D. F. Jankowski, M. K. Smith, A. Glezer & M. Schatz and the assistance of colleagues at the Microgravity Advanced Research Support Centre in Naples, Italy and in the School of Physics at the Georgia Institute of Technology. This research was sponsored by the Microgravity ~~Science and Applications~~ Division within the Office of Life and Microgravity Sciences of NASA. and Research

REFERENCES

Ben Hadid, H. & Roux, B. 1990 Thermocapillary convection in long horizontal layers of low-Prandtl-number melts subject to a horizontal temperature gradient. *J. Fluid Mech.* **221**, 77.

Benz, S., Hintz, P., Riley, R. J. & Neitzel, G. P. 1998 Instability of thermocapillary–buoyancy convection in shallow layers. Part 2. Suppression of hydrothermal waves. *J. Fluid Mech.* **000**, 000–000.

Chun, C.-H. & Wuest, W. 1979 Experiments on the transition from the steady to the oscillatory Marangoni-convection of a floating zone under reduced gravity effect. Acta Astr. 6, 1073.

missing reference

Cramer, A., Schneider, J. & Schwabe, D. 1997 On the transition from mono- to multiroll thermocapillary convection in shallow layers. *J. Fluid Mech.* (submitted for publication).

Daviaud, F. & Vince, J. M. 1993 Traveling waves in a fluid layer subjected to a horizontal temperature gradient. *Phys. Rev.* E **48**, 4432.

Davis, S. H. & Homsy, G. M. 1980 Energy-stability theory for free-surface problems: buoyancy-thermocapillary layers. *J. Fluid Mech.* **98**, 527.

De Saedeleer, C., Garcimartin, A., Chavepeyer, G. & Platten, J. K. 1996 The instability of a liquid layer heated from the side when the upper surface is open to air. *Phys. Fluids* **8**, 670.

Ezersky, A., Garcimartin, A., Mancini, H. L. & Perez-Garcia, C. 1993 Spatiotemporal structure of hydrothermal waves in Marangoni convection. *Phys. Rev.* E **48**, 4414.

Garr-Peters, J. M. 1992*a* The neutral stability of surface-tension driven cavity flows subject to buoyant forces–I. Transverse and longitudinal disturbances. *Chem. Engng. Sci.* **47**, 1247.

Garr-Peters, J. M. 1992*b* The neutral stability of surface-tension driven cavity flows subject to buoyant forces–II. Oblique disturbances. *Chem. Engng. Sci.* **47**, 1265.

Gatos, H. C. 1982 Semiconductor crystal growth and segregation problems on earth and in space. In *Materials Processing in the Reduced Gravity Environment of Space*. (ed. G. E. Rindone). Elsevier.

Kirdyashkin, A. G. 1984 Thermogravitational and thermocapillary flows in a horizontal liquid layer under the conditions of a horizontal temperature gradient. *Int. J. Heat Mass Transfer* **27**, 1205.

Levenstam, M. & Amberg, G. 1995 Hydrodynamical instabilities of thermocapillary flow in a half-zone. *J. Fluid Mech.* **297**, 357.

Mercier, J. F. & Normand, C. 1996 Buoyant-thermocapillary instabilities of differentially heated liquid layers. *Phys. Fluids* **8**, 1433.

Neitzel, G. P., Chang, K.-T., Jankowski, D. F. & Mittelmann, H. D. 1993 Linear-stability theory of thermocapillary convection in a model of the float-zone crystal-growth process. *Phys. Fluids* A **5**, 108.

Neitzel, G. P., Law, C. C., Jankowski, D. F. & Mittelmann, H. D. 1991 Energy stability of thermocapillary convection in a model of the float-zone crystal-growth process. II: Nonaxisymmetric disturbances. *Phys. Fluids* A **3**, 2841.

Parmentier, P. M., Regnier, V. C. & Lebon, G. 1993 Buoyant-thermocapillary instabilities in medium-Prandtl-number fluid layers subject to a horizontal temperature gradient. *Intl. J. Heat Mass Transfer* **36**, 2417.

Preisser, F., Schwabe, D. & Scharmann, A. 1983 Verification of the oscillatory state of thermocapillary convection in liquid columns with free cylindrical surface. *J. Fluid Mech.* **126**, 545.

Riley, R. J. 1995 An investigation of the stability and control of a combined thermocapillary-buoyancy driven flow. PhD thesis, Georgia Institute of Technology.

Riley, R. J. & Neitzel, G. P. 1998 Linear-stability of buoyancy-thermocapillary convection in shallow layers. *in preparation*

Schwabe, D., Möller, U., Schneider, J. & Scharmann, A. 1992 Instabilities of shallow dynamic thermocapillary liquid layers. *Phys. Fluids* A **4**, 2368.

Schwabe, D., Scharmann, A., Preisser, F. & Oeder, R. 1978 Experiments on surface tension driven flow in a floating zone melting. *J. Cryst. Growth* **43**, 305.

Sen, A. K. & Davis, S. H. 1982 Steady thermocapillary flows in two-dimensional slots. *J. Fluid Mech.* **121**, 163.

Shen, Y., Neitzel, G. P., Jankowski, D. F. & Mittelmann, H. D. 1990 Energy stability of thermocapillary convection in a model of the float-zone crystal-growth process. *J. Fluid Mech.* **217**, 639.

Smith, M. K. 1986 Instability mechanisms in dynamic thermocapillary liquid layers. *Phys. Fluids* **29**, 3182.

Smith, M. K. 1988 The nonlinear stability of dynamic thermocapillary liquid layers. *J. Fluid Mech.* **196**, 391.

Smith, M. K. & Davis, S. H. 1983 Instabilities of dynamic thermocapillary liquid layers. Part 1. Convective instabilities. *J. Fluid Mech.* **132**, 119.

Velten, R., Schwabe, D. & Scharmann, A. 1991 The periodic instability of thermocapillary convection in cylindrical liquid bridges. *Phys. Fluids* A **3**, 267.

VILLERS, D. & PLATTEN, J. K. 1992 Coupled buoyancy and Marangoni convection in acetone: experiments and comparison with numerical simulations. *J. Fluid Mech.* **224**, 487.

WANSCHURA, M., SHEVTSOVA, S., KUHLMANN, H. C. & RATH, H. J. 1995 Convective instability mechanisms in thermocapillary liquid bridges. *Phys. Fluids* **7**, 912.

H 145.55 RM
16 pages

J. Fluid Mech. (1998), *vol.* 35X, *pp.* 1–16. Printed in the United Kingdom

CAMBRIDGE UNIVERSITY PRESS
TEX ARTICLE
PLEASE RETURN THIS PROOF DJS

Instability of thermocapillary–buoyancy convection in shallow layers. Part 2. Suppression of hydrothermal waves

By S. BENZ[1], P. HINTZ[1], R. J. RILEY[2] AND G. P. NEITZEL[3]

[1]Physikalisches Institut, Universität Gießen, Germany
[2]Cabot Corporation, Research and Development, Pampa, TX 79066, USA.
[3]The George W. Woodruff School of Mechanical Engineering, Georgia Institute of Technology, Atlanta, GA 30332-0405, USA

(Received 5 October 1996 and in revised form 12 November 1997)

f.o.

Hydrothermal-wave instabilities in thermocapillary convection are known to produce undesirable effects when they occur during the float-zone crystal-growth process, and perhaps in other situations. Suppression of the hydrothermal-wave instability produced in the model system of Part 1 (Riley & Neitzel 1998) is demonstrated through the sensing of free-surface temperature perturbations and the periodic addition of heat at the free surface along lines parallel to the crests of the hydrothermal waves.

1. Introduction

The onset of oscillatory thermocapillary convection during the float-zone crystal-growth process is thought to be responsible for the appearance of undesirable striations in material resulting from the process. This is shown convincingly in experiments reported by Gatos (1982), in which the heater current was oscillated during crystal growth from melt and dopant striations observed in the resulting crystal could be correlated with the imposed temporal oscillations. Analyses of the stability of thermocapillary convection in half-zone models of the float-zone process, such as those performed by Shen *et al.* (1990), Neitzel *et al.* (1991), Wanschura *et al.* (1995) and Levenstam & Amberg (1995), yield results which identify regions of either guaranteed stability (energy theory) or guaranteed instability (linear theory). In the case of an actual crystal-growth situation, such results (were they even available) may not be of practical utility, since the crystal grower has little latitude in setting operating conditions to, say, keep the Marangoni number within a region known to be free of instability. In such a situation, it may be worthwhile to explore the possibility of suppressing oscillatory thermocapillary convection, should it occur. This provides the motivation for the present work.

Riley & Neitzel (1998) (hereafter referred to as Part 1) have experimentally demonstrated the existence of the hydrothermal-wave instability predicted by Smith & Davis (1983) in thin layers of silicone oil for which buoyancy forces are quite small. This instability is characterized by the appearance of a single family of thermal waves which propagate obliquely across the layer at an angle which depends on the Prandtl number of the liquid. Smith (1986) has discussed the instability mechanism for this convective instability: for the high-Prandtl-number case appropriate to the oil used in the experiments of Part 1, there is an interaction between the temperature fluctuations on the free surface and the bulk temperature which sustains the hydrothermal waves. Hence, interference with this mechanism through the modification of the free-surface temperature may provide a way to delay the onset of the undesirable oscillations. For the case of classical Rayleigh–Bénard convection, Tang & Bau (1993) have demonstrated theoretically the possibility of delaying the onset of convection significantly through local modification of the temperature of the bottom wall.

Additional motivation for undertaking an approach of this type is provided by the experiments of Liepmann, Brown & Nosenchuck (1982) and Liepmann & Nosenchuck (1982), who used periodic surface strip heating to suppress the growth of both artificially induced disturbances and naturally occurring Tollmien–Schlichting (T–S) waves in a laminar boundary layer on a flat plate. In the latter case, the appearance of T–S waves was delayed significantly. These experiments were performed in water and the periodic heating, through the reduction of viscosity, mimicked the action of periodic suction at the wall. The actuation of the heating was provided by the signal from an upstream wall-shear-stress sensor.

7

The present experiments utilize the ideas employed by Liepmann & Nosenchuck (1982), along with the theoretical basis provided by Smith (1986), to demonstrate that suppression of hydrothermal waves is possible in thin layers dominated by thermocapillarity. Sensing of free-surface temperature fluctuations is accomplished non-intrusively in real time using an infrared (IR) camera. Surface heating is delivered to the layer in the form of a thin sheet of infrared radiation from a CO_2 laser which is out of phase with the temperature fluctuations associated with the hydrothermal waves at the location of the sheet. Nahas & Panton (1990) have used a similar technique to drive opposing flows on the surface of a jet undergoing acoustically forced capillary breakup, thus delaying the formation of droplets. Recently, Petrov *et al.* (1996) have employed a nonlinear control algorithm using temperature measurements near the free surface and heating with a thermoelectric element to suppress oscillations of thermocapillary convection in liquid bridges.

2. Experimental setup and procedure

The apparatus employed for these experiments is the same as used in the experiments reported in Part 1; figure 1 of that paper provides a sketch of the geometry of the layer. To demonstrate the feasibility of control, we concentrate on the suppression of hydrothermal waves for a layer $d = 1$ mm in depth, corresponding to axial (L/d) and transverse (W/d) aspect ratios of 30 and 50, respectively, and a dynamic Bond number of $Bo_D = 0.142$.

The output of the CO_2 laser is focused and formed into a sheet which is used to heat a line of small thickness on the free surface of the liquid layer downstream (with respect to the wave-propagation direction) of the thermocouple locations at which input data characterizing each hydrothermal wave are collected. The plan is to selectively heat the troughs of disturbance temperature, thereby locally raising the temperature there and hopefully disrupting the instability mechanism described by Smith (1986).

The control of a particular hydrothermal wave is achieved using data measured specifically for that wave, necessitating the use of a delay in the *feed-forward control* scheme to be described. The signal from the infrared camera described in Part 1 is first converted into a video signal, which is output to a video-cassette recorder (VCR) for recording and to a frame grabber for real-time analysis. The images from

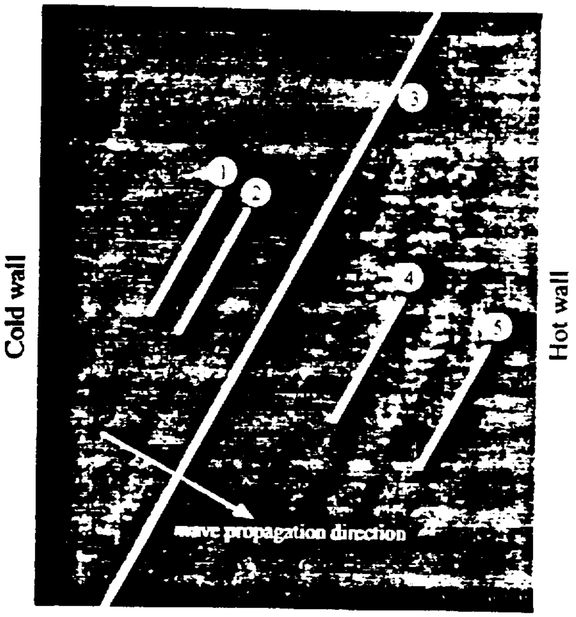

FIGURE 1. Overhead view of layer, showing hydrothermal waves and locations of data (1, 2, 4 and 5) and heating (3) lines.

the frame grabber are processed in the following fashion, illustrated in figure 1, to initiate the control. Two lines (identified by the numerals 1 and 2 in figure 1) which (5) are parallel to the observed hydrothermal-wave crests and located upstream of the known control site (line 3 in figure 1) are selected as input data locations. Along these lines, each of which occupies 79 pixels, the luminance data are averaged to smooth the noise resulting from pixel-to-pixel variations. The 79-pixel line length is the longest line which can be used and still perform the control in real time, given the limitations of the computer employed. The time histories of these averaged signals are used to compute the phase speed of each hydrothermal wave which passes. The distance between lines 1 and 2 is less than the wavelength of a hydrothermal wave so there is no ambiguity in the determination of this phase speed. As mentioned above, downstream of lines 1 and 2 is a line identified by 3 placed at the location where the laser heating is to be delivered.

The *output signal* to the laser controller is created in the following fashion. The line-averaged luminance signal from line 2, called the *raw input signal*, is jump-limited and drift compensated using a running time mean. A constant input gain and a constant offset (which are set manually at the beginning of every experiment) are applied to this signal to shift it into a window (with a value range [−1, 1]) that is suitable for further processing and monitoring on an oscilloscope. This processed input signal is then temporarily stored in a buffer, so that the output signal may be delayed to allow for the hydrothermal-wave transit time between lines 2 and 3. Data read from the buffer at a location corresponding to the proper time delay are then inverted, gain adjusted and offset to construct an output signal within the 0–10 V range required by the laser controller. This output signal, tailored to each passing hydrothermal wave, allows the delivery of laser heating to each hydrothermal-wave temperature trough to suppress the oscillations. Lines 4 and 5 in figure 1 are used for the collection of data used to assess the effectiveness. Output gain and offset may be varied manually during experiments in order to investigate the effect of the magnitude of laser power on the control.

A previous attempt at control was made by Riley (1995) using a fine-wire thermocouple placed near the corner of the flow field from which the hydrothermal waves appear to emanate. The signal coming from the thermocouple was inverted, gain adjusted, phase shifted and sent to the laser controller, as above, but the phase shift of the signal had to be adjusted manually due to a lack of knowledge of the phase speed of the waves. The initiation of control was found to be extremely sensitive to this choice of phase shift. When wave suppression was achieved, it was not possible for it to be maintained for more than roughly a half dozen cycles, due to a combination of factors. First, the advection of a portion of the laser energy to the thermocouple location through the vigorous free-surface motion of the basic state causes a change in the signal there. Secondly, slight modification of the wave pattern upstream of the control location is observed following the successful initiation of suppression which necessitates a further change in phase shift of the laser input. The manual setting of this phase shift, coupled with the sensitivity of the system to its choice, did not permit this adjustment to be made, as it is automatically with the present scheme. Therefore, although this intrusive scheme was able to demonstrate that wave suppression is possible for at least a few cycles, data from a single-point measurement are not sufficient to permit tailoring the control scheme to specific waves, as described above.

In implementing the present control scheme described above, there are a couple of points to keep in mind. First, as mentioned in the previous paragraph, the free-surface flow is in a direction opposite to that of the streamwise component of the phase velocity of the hydrothermal waves and is large compared with the phase speed. For instance, for the case considered in this paper, the free-surface speed of roughly 7 cm s^{-1} is relatively large compared with the hydrothermal-wave phase speed of approximately 2 mm s^{-1}. Hence, for the 1 cS silicone oil ($Pr = 13.9$) used in these experiments, large temperature changes created by the laser heating can be advected to the read lines (1 and 2 in figure 1), potentially degrading the quality of the input signal necessary to accomplish the suppression. Second, the hydrothermal waves which appear following the onset of instability are large everywhere in the flow domain (see also figures 8 and 9 of Part 1). On the other hand, the T–S waves of interest in the Liepmann & Nosenchuck (1982) experiment are convective in nature, growing in the flow direction. The hydrothermal-wave instability thus appears somewhat reminiscent of an absolute instability in character, which may have further negative implications from the standpoint of suppression, particularly if the absence of oscillatory flow is required everywhere in the layer.

Figure 2 shows an overall schematic of the control experiment. The laser employed for these experiments is a Synrad (48-1-115W) CO_2 laser, with variable output power ranging from 0 to 10 W at 10.6 μm, which is controllable with an analog input voltage between 0 and 10 V. The laser beam has a nominal diameter of 3.5 mm, but is allowed to expand in this experiment for slightly less than 2 m to assure the existence of a Gaussian beam. Once expanded, the beam (now 7 mm in diameter) passes through a 3 mm diameter aperture and is directed toward the flow apparatus by an angled mirror. It then passes through a zinc-selenide lens with a 250 mm focal length before being reflected by a concave cylindrical mirror with a focal length of −12.7 mm. This mirror serves to redirect the beam downward toward the free surface of the liquid and simultaneously expand it into a sheet. This sheet of 10.6 μm infrared radiation intersects the free surface of the liquid, producing the desired line-heating source for the control output.

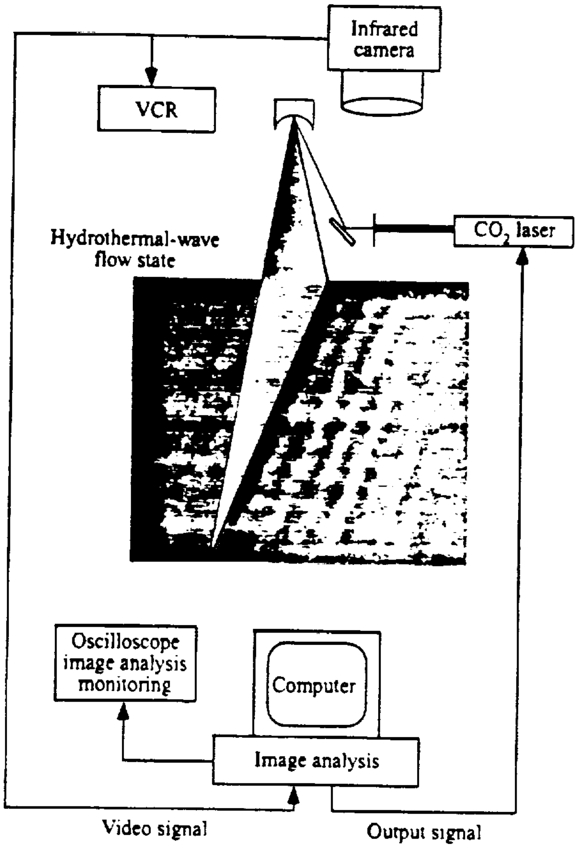

FIGURE 2. Schematic of the control experiments.

For the control scheme to be successful, the thickness of the infrared sheet can be no greater than one-half of the wavelength of the hydrothermal waves. Since a 1.0 mm deep layer is investigated in these control experiments, and the experimentally determined critical wavelength for that depth is $\lambda = 2.58$ mm (table 2, Part 1), a sheet thickness of about 1 mm is desired. In order to measure this thickness, a piece of Plexiglas is heated and observed using the infrared camera. A graph of the line luminance normal to the heated line is shown in figure 3. From this profile, the estimated full-width-at-half-maximum sheet thickness is 1.14 mm, which is less than one-half of the disturbance wavelength for the layer examined in these experiments. This measurement technique should yield a relatively good estimate for the laser-sheet thickness. In the limit of zero thermal conductivity, the image of the heated area yields the true sheet thickness since the heat does not diffuse away from the line of application. Since Plexiglas has a relatively low thermal conductivity, the thickness determined in this fashion is only slightly greater than the true sheet thickness of the infrared sheet.

Since the CO_2 beam is invisible, the alignment of the optical system is a non-trivial undertaking. Optical alignment is accomplished by placing strips of Plexiglas in the optical path, and burning them with the beam. This allows the alignment of each optical component with the burned spot. Once the beam is finally expanded into a sheet, a rough alignment with the flow apparatus is performed using thermally

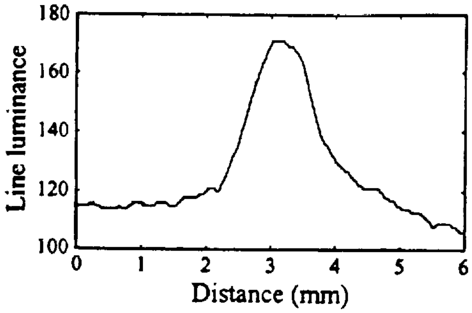

FIGURE 3. Line-luminance trace across a heated line on a Plexiglas surface.

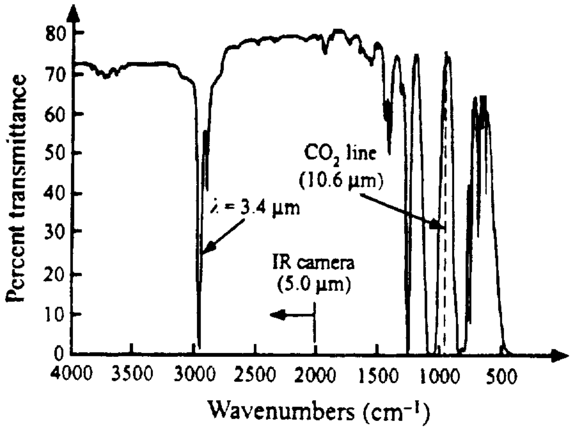

FIGURE 4. Absorption spectrum from a smear sample of 1 cS silicone oil.

sensitive beam-probe plates in conjunction with an ultraviolet light source. Final alignment of the sheet with respect to the obliquely propagating hydrothermal waves is accomplished using the infrared camera described in Part 1 to locate the position and orientation of the heated line with the hydrothermal wave pattern present in -⁁
the flow apparatus. Since either of two possible wave families may appear (Smith & Davis 1983), a mechanism allows the concave mirror to be rotated to always allow 7
heating parallel to the wave crests of the observed family.

A final note on the experimental setup and data collection concerns the absorption properties of 1 cS Dow Corning 200 silicone oil. Figure 4 shows an absorption spectrum of a smear sample of 1 cS silicone oil measured by colleagues in the Georgia Institute of Technology School of Chemistry and Biochemistry. Two absorption bands of importance are marked in the figure. The band at 3.4 μm is what is 'seen' by the infrared camera, and the line at 10.6 μm denotes the wavelength of the CO$_2$ laser corresponding to the heating. The camera is virtually insensitive to anything to the right of the line marked at 5.0 μm. This is important, because it allows the camera to detect the thermal field in the liquid, without being blinded by the much stronger laser emission at 10.6 μm. However, the fact that a heated line on the surface of the fluid layer appears as a dark stripe (see figure 5*d*) indicates that some of the reflected radiation at 10.6 μm is picked up by the IR-camera. Also note that the absorption at 10.6 μm is relatively weak, but since this spectrum is collected for a smear sample the implication of this is uncertain. The data of Pline (1989) for 10 cS silicone oil display a very similar spectrum to that measured for the 1 cS oil, and absorption results for a 100 μm-thick liquid sample indicate nearly total absorption. If one assumes similar results to hold for the 1 cS oil used in the present experiments, one would conclude that the heating of the liquid at the free surface actually occurs in a thin layer ~~beneath~~ at the free surface of roughly 100 μm thickness. For a total layer depth of 1 mm, this would imply that the 'surface' heating in these experiments occurs within the top 10% of the liquid layer. We shall see in §3, however, that subsequent measurements indicate that this may not be the case.

3. Results and discussion

The control scheme described above was applied to suppress hydrothermal waves for a 1 mm deep layer at a laboratory Marangoni number of approximately $Ma_L \approx 575$. The critical Marangoni number corresponding to this layer depth presented in Part 1 is $Ma_L = 440$, so that this layer is substantially supercritical. In addition to the technique just described of pulsing the laser using the signal from the upstream waves, the influence of a constant laser power is also investigated. The effectiveness of the control is assessed by examining line-averaged pixel luminance data in thermographic images which correspond to free-surface temperature fluctuations at locations both upstream and downstream of the control site. For all thermographs presented in this paper, the cold and hot walls of the apparatus are at the left- and right-hand sides, respectively, and the hydrothermal waves propagate from upper-left to lower-right.

3.1. *Time-dependent heating*

This technique is the one described in §2 above, whereby the time-dependent laser power delivered to the IR sheet is adjusted based on the signals from the data read lines (lines 1 and 2 in Figure 1). The magnitude of the laser power delivered to the fluid layer is controlled by manually setting the values for output-signal gain and offset. By properly setting these two parameters it is assured that the output-signal troughs are very close to zero, meaning that virtually no heat is delivered to the high-surface-temperature locations of the hydrothermal waves. Also, by adjusting output gain and offset in such a fashion, the relative differences between the peak-to-peak and the zero-to-peak amplitudes of the output signal can be reduced to less than 10%.

Figure 5 shows four instantaneous thermographs of the layer free surface taken while operating in this mode. The image in figure 5(*a*) is of the layer prior to initiating control, showing pure hydrothermal waves. Dark regions correspond to cold spots, while light regions indicate high surface temperature. In figure 5(*b*), control is attempted with the laser set at an intermediate power level. Some attenuation of waves is visible downstream from the heating location with hydrothermal wave suppression being stronger in the vicinity of the hot wall. As depicted in figure 5(*c*) this tendency is enhanced as the laser power is increased. Finally, for the power level used in figure 5(*d*), the thermograph is shown at an instant when the laser power is near its maximum so that the location of the heating line is also clearly visible.

From a visual inspection of these thermographs, it is clear that the application of the technique has resulted in the disappearance of hydrothermal waves downstream of the heating location. Figure 6, however, shows evidence of the effectiveness of the control of a more quantitative nature. In figure 6(*a*), the time histories of the line-averaged luminance from lines 2 and 4 are plotted for a case prior to the initiation of control; in figure 6(*b*) the same quantities are shown after the start of periodic heating at a power

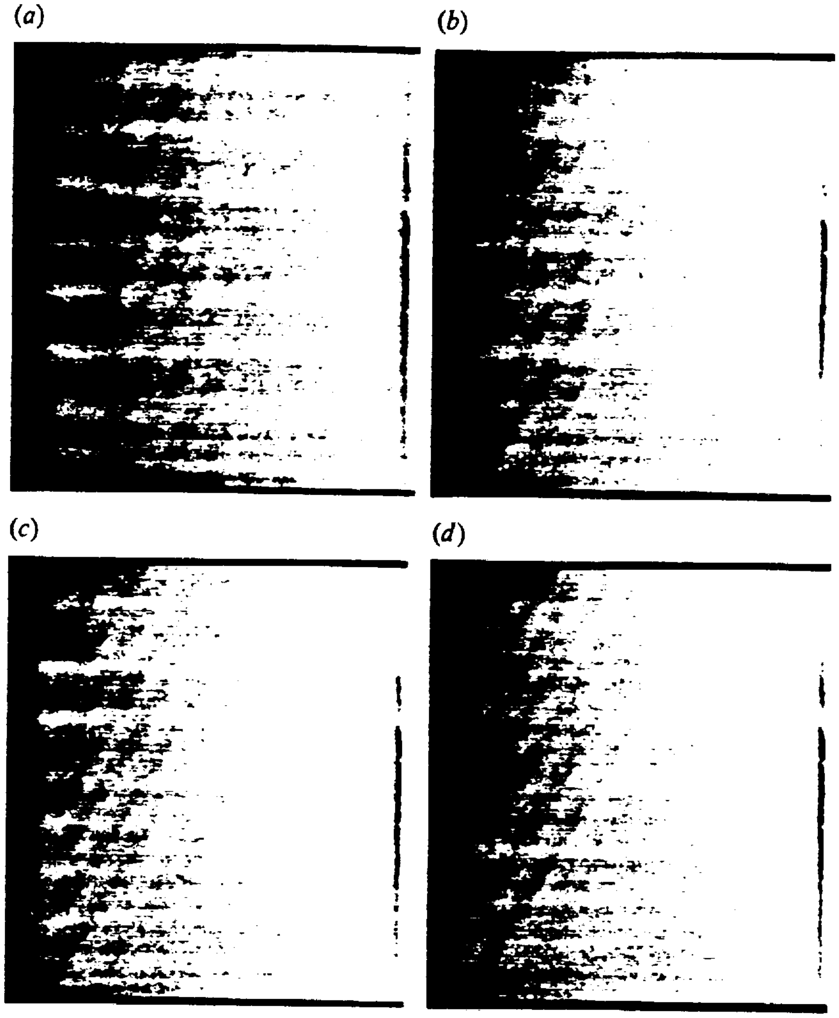

FIGURE 5. Infrared thermographs showing effectiveness of the time-dependent control scheme at various laser-aperture power (zero-to-peak) levels: (*a*) 0 W; (*b*) 1.3 W; (*c*) 2.2 W; (*d*) 3.3 W.

level which corresponds to the state shown in figure 5(*d*). It may be observed that the line 2 data are slightly affected (a small amplitude increase may be observed) by the application of periodic heating, while the peak-to-peak amplitude of the signal at line 4 has been reduced through control from a line-averaged luminescence of roughly ~~five~~ to one of $O(0.5)$, which is within the data noise level (determined from Fourier spectra to be discussed in the next paragraph). Control is achieved within roughly 30–45 s of turning on the laser and may be maintained virtually indefinitely. As noted in §2, earlier experiments performed using a single-point intrusive thermocouple (Riley 1995) to initiate the laser were only successful in obtaining a few cycles of control, due to a combination of a lack of knowledge of the hydrothermal-wave phase speed and to feedback from the heating line to the thermocouple.

5 /

(use of 'five' is confusing since it is almost immediately followed by the word 'one'.)

The influence of laser power level on control was investigated using an experimental protocol which manually stepped the laser power from zero in variable increments of $O(0.5\ \mathrm{V})$ peak-to-peak, holding the laser power at each level for roughly ~~3~~ minutes.

three /

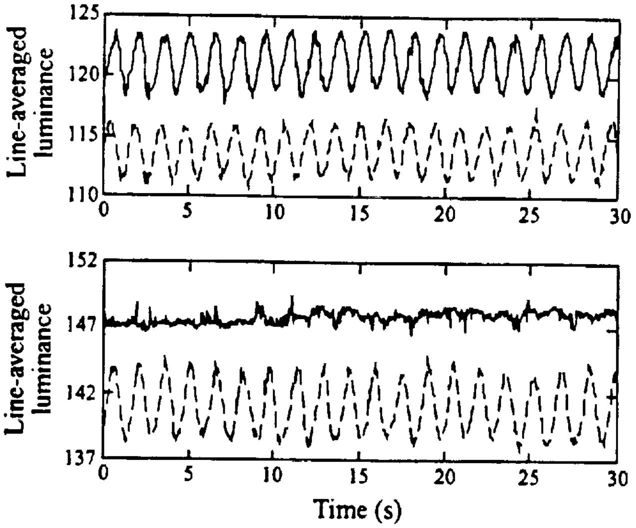

FIGURE 6. Line-averaged luminance from upstream (line 2 ∤ dashed) and downstream (line 4 ∤ solid) data-read lines for the time-dependent control scheme: (*a*) no control (data from line 4 have been offset by a luminance value of 38 to allow both curves to be displayed together); (*b*) laser-aperture power (zero-to-peak) of 3.3 W, corresponding to the thermograph seen in figure 5(*d*) (data from line 4 have been offset by a luminance value of 45 to allow both curves to be displayed together).

② —

This is more than enough time for the flow to accommodate to the new power, as verified from examining the Fourier spectra computed at different time intervals within the ~~three~~-minute window (the transition time seen in the Fourier analysis is around 30 to 45 s). The following results are based on the amplitudes of the primary Fourier modes, taken during the last 37 s of these windows. Line-averaged luminance data are gathered at a rate of 15 Hz at each of lines 1, 2, 4 and 5 of figure 1. To determine the dominant component, thirty-one Fourier transforms are computed on a sliding data set of 256 consecutive data points. Since a discrete Fourier transform is employed, the observed oscillations do not consist of a pure mode, i.e. with all power in a single Fourier component. Rather, the vast majority of the power is always contained in two adjacent modes which correspond to frequencies of 0.59 and 0.64 Hz. The mean value of these two Fourier components is nearly constant during the 37 s period at the end of the 3-minute data window. Therefore, the analysed data correspond to a state, which, after the previous increase of laser power, has relaxed to a new equilibrium. The mean of these two largest Fourier amplitudes, is further time-averaged over the 37 s data-analysis window and reported as the 'Fourier amplitude' in what follows. Figure 7(*a*) shows the variation of this Fourier amplitude as a function of zero-to-peak voltage delivered to the laser at each of lines 1, 2, 4 and 5 for a single experiment. Lines marked as (i)–(iv) on this figure correspond to the power levels employed in the experiments which produced the thermographs in figure 5(*a*)–(*d*), respectively. At a power level slightly below 1 V, the amplitude at the downstream lines (4 and 5) begins to decrease, indicative of the effectiveness of the heating in suppressing the hydrothermal waves.

3

Also observed in figure 7(*a*) is an upward drift in Fourier amplitude at the upstream lines (1 and 2). This was mentioned in the discussion of the line 2 data from figure 6. While the precise cause for this behaviour is not known for certain, some reasons may be speculated. The heating at line 3 is observed to raise the mean temperature

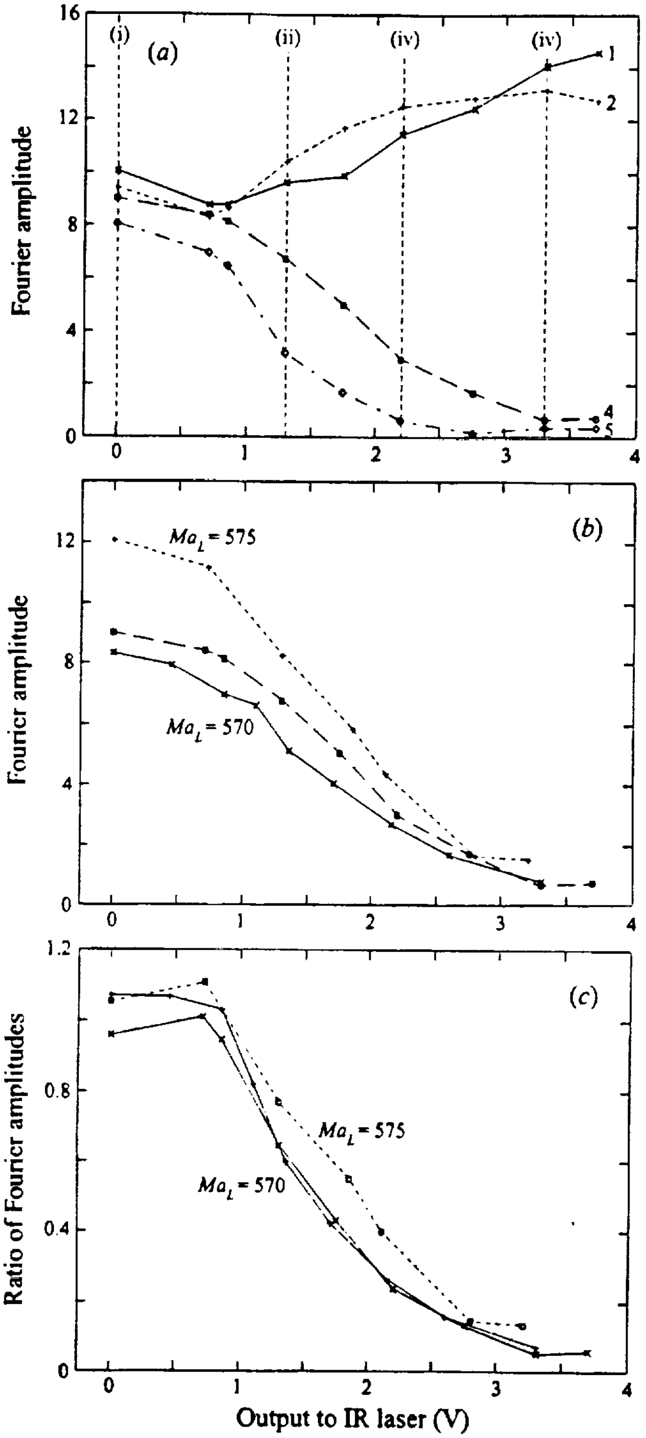

FIGURE 7. Spectral evaluation of the influence of laser power for the time-dependent control scheme: (a) single experiment, showing the behaviour at the four data-read lines (vertical lines show the power levels corresponding to those of figure 5); (b) line 4 data from three different sets of experiments; (c) line 4 data from three different sets of experiments normalized by the corresponding line 2 data upstream of the heating location.

of the fluid at locations 1 and 2, but this has no direct effect on the values plotted in figure 7(*a*) because only the pair of dominant modes of the oscillatory component are being shown there (only the Fourier components corresponding to 0.59 Hz and 0.64 Hz are considered, as discussed above). A possible indirect effect, however, may be important since the increase of mean temperature at lines 1 and 2 results in a slight increase of the time-averaged local temperature gradients upstream from the heating line (recall that lines 1 and 2 are near the cold wall of the apparatus). Therefore, the local Marangoni number *Ma* discussed in Part 1 is increased as laser power increases, and this fact could possibly explain the increases observed in the line 1 and 2 values. During the experiments which produced the hydrothermal waves reported here (i.e. in the range $450 < Ma_L < 570$), it is found that the amplitude of hydrothermal waves does increase with increasing Marangoni number. A systematic investigation to determine the amplitude of these free-surface temperature fluctuations and their dependence on experimental parameters has not been performed, hence the above discussion remains ~~hypothetical~~. speculative

In figure 7(*b*), results of line 4 data are shown for three different sets of experiments, indicating the reproducibility of the influence of laser power level. From these curves, one might mistakenly conclude that the amplitude of the surface-temperature fluctuations at $Ma_L = 575$ is somewhat larger than at $Ma_L = 570$. However, this conclusion cannot be drawn. The values plotted in figure 7(*b*) are a quantitative measure of the luminance variations in the analysed infrared images which depend linearly ~~dependenced~~ on the surface temperature variations. The linear dependence is determined by the infrared image gain and offset, two parameters that are set manually in the infrared camera controller and were varied from experiment to experiment. The somewhat larger values plotted in figure 7(*b*) at $Ma_L = 575$ result from using a larger infrared image gain in that particular experiment. The increase of hydrothermal-wave amplitude with Marangoni number which was mentioned earlier therefore does not emerge from figure 7(*b*). Perhaps the most instructive and independent of assessment parameters is the relative attenuation of the hydrothermal waves shown in figure 7(*c*), where the line 4 data are scaled by the respective amplitudes at line 2 for each laser power.

It is clear that the degree of amplitude reduction is directly correlated with power supplied to the laser. Further, at a power level of about 2.5–3 V, the luminance oscillation amplitudes have disappeared into the noise level, indicating that maximum possible control has been achieved.

3.2. *Constant heating*

For this set of experimental trials, the positions of all lines in figure 1 were left unchanged from those of the time-dependent-heating case. The difference is that, for these experiments, the heating provided by the laser is constant in time, manually set to different values to again assess the influence of laser power. Therefore, the entire active-control algorithm described above is bypassed. Lines 1, 2, 4 and 5, however, are still used to record data for the purposes of evaluation.

Figure 8 shows the behaviour of the dominant oscillatory Fourier component of the line-averaged luminance at lines 1, 2, 4 and 5 as a function of laser power for a single experiment. For low-to-moderate values of laser power the behaviour of these modes is reminiscent of what is observed in the time-dependent cases: for low enough values of the laser power, control is absent; as power increases, attenuation of the Fourier mode is seen at the locations downstream of the heating line. What is different in these experiments, however, is the fact that signal attenuation is also

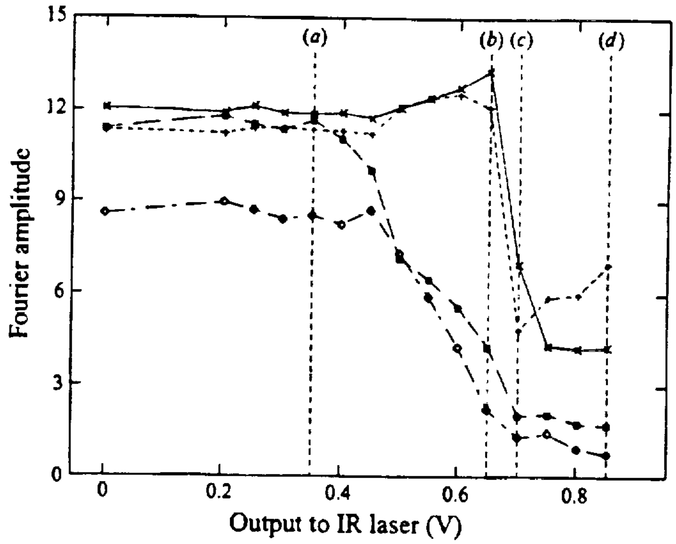

FIGURE 8. Spectral evaluation of the influence of laser power for the constant-heating control scheme for a single experiment, showing the behaviour at the four data-read lines (vertical lines show the power levels corresponding to those of figure 9).

observed upstream (lines 1 and 2) of the heating line for large enough values of laser power, suggesting that the influence of the constant heating may be to suppress waves everywhere in the layer. This, however, is not actually the case, as the following discussion shows.

Figure 9 shows a sequence of four thermographs of the layer corresponding to different magnitudes of constant laser heating; the four corresponding power levels are indicated on figure 8 by the letters (*a*), (*b*), (*c*) and *d* respectively. At the lowest of the continuous-power levels seen in figure 9(*a*), the heating at line 3 has no visible effect on the hydrothermal waves. Figure 9(*b*) shows a thermograph taken at a somewhat higher laser power level at which some suppression of wave behaviour in the vicinity of the heating line can be noticed. This is contrary to what is observed at lower power levels in the time-dependent case, where suppression is observed closer to the hot wall, moving toward the heating line as power is increased. Note that the steady output voltages employed in the constant-heating experiments are much smaller (by a factor of 5; see figures 7 and 8) than those (zero-to-peak) used in the time-dependent control scheme. As laser power is increased to the value corresponding to the thermograph in figure 9(*c*), the wave structure at locations upstream of the line has lost some of the regularity observed for lower power levels and a clear change in the propagation angle of the upstream waves is evident. Finally, the thermograph of figure 9(*d*) corresponds to a power level for which the spectral results in figure 8 indicate a strong attenuation of waves downstream from the heating location but also a greatly reduced amplitude upstream. However, upstream of the heating line a well-defined group of waves is visible in the thermograph, but at a different angle than those observed for lower heating. The misalignment of these wave crests with read lines 1 and 2 now means that the line averages along these lines will cross wave crests, yielding a smaller fluctuating value, reflected in the reduced magnitude of the Fourier component.

(d)/

As discussed above for the case of time-dependent heating, the application of steady

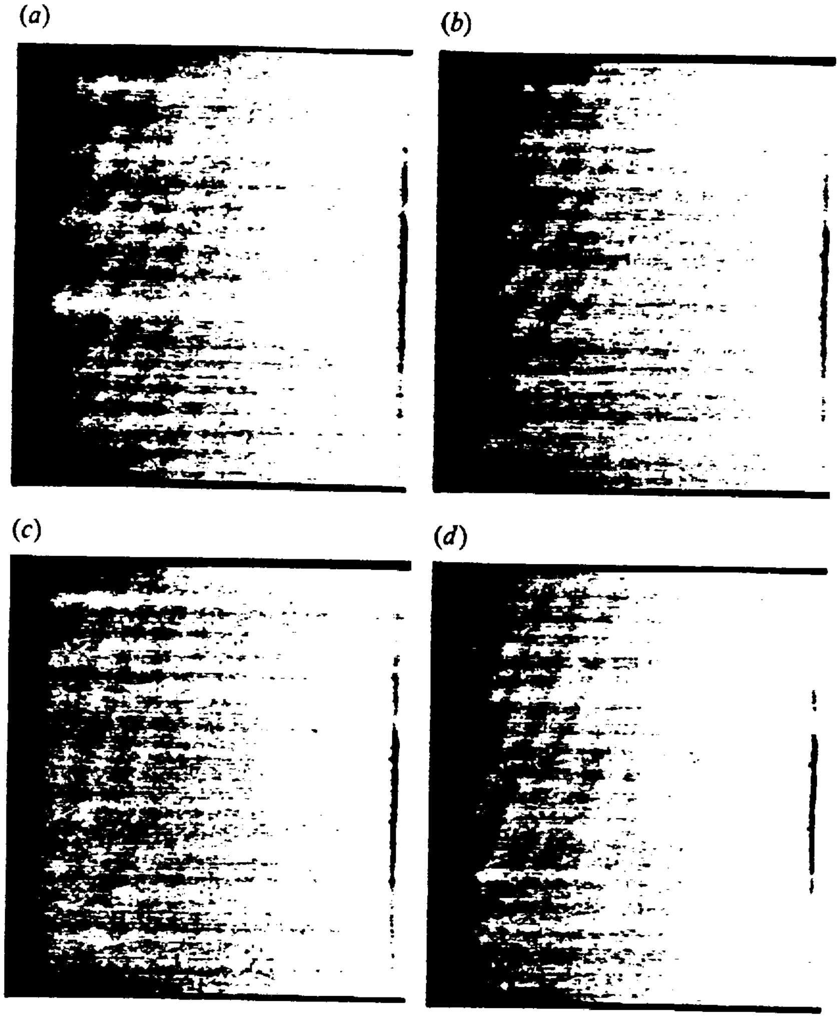

FIGURE 9. Infrared thermographs showing effectiveness of the constant-heating control scheme at various laser-aperture power (zero-to-peak) levels: (*a*) 0.35 W; (*b*) 0.65 W; (*c*) 0.7 W; (*d*) 0.85 W

heating undoubtedly affects the structure of the basic state itself. In particular, the mean-temperature gradient between line 3 and the hot wall is reduced by the heating; consequently, the local Marangoni number *Ma* in this region is reduced. As *Ma* is reduced, the amplitude of hydrothermal waves will decrease; if *Ma* falls below the critical value for the onset of hydrothermal waves, then waves should not appear there, and this is the likely reason for their observed disappearance. Therefore, it appears that steady power levels supplied to the layer in this manner have changed the underlying structure of the basic state, and hence, the instability. This is not the case with time-dependent heating. Evidence of this is provided by the earlier experiments performed using a thermocouple as the source of the input signal. As mentioned in §2 and §3.1, these experiments were extremely sensitive to the manually chosen phase shift: if this was not selected properly, hydrothermal waves covered the entire free surface, both upstream and downstream of the heating, in spite of the fact that heating was being applied. Also, following the loss of control in those experiments, waves reappeared at both upstream and downstream locations. If the periodic heating were affecting the layer in the same manner as in the constant-heating experiments, one would expect the downstream waves to be absent, which was not the case. Consequently, the application of steady heating parallel to the crests of the originally appearing hydrothermal waves is perhaps a less attractive way to achieve control than the time-dependent scheme described in §3.1.

3.3. *Energy transmission estimate*

In addition to obtaining these results, an energy balance was performed to estimate the effect of the incident radiation. From the results of Pline (1989) for 10 cS silicone oil, it was estimated the majority of the absorbed energy at the 10.6 μm emission line is absorbed in a layer of roughly 100 μm thickness. Thus, the volume of fluid which absorbs radiation from the CO_2 laser is equal to the surface area which is exposed multiplied by the 100 μm thickness of the absorption layer. The time during which the heating is active is that time necessary for the local temperature depression to pass the heating line, which, for the case of a 1.0 mm-deep layer at the critical Marangoni number, is approximately $\Delta t = 0.8$ s. An approximate energy balance yields

$$\rho c_p V \Delta T = \overline{Q}_{abs} \Delta t - \dot{m} c_p (\overline{T}_{out} - \overline{T}_{in}),$$

i.e.

where the term on the left-hand side represents the temperature rise of the liquid volume under the applied radiative flux, the first term on the right-hand side is the radiative energy absorbed by the layer, and the last term is the energy convected out of the control volume. Conductive and radiative losses from the layer have been neglected as they are small, and any additional convection induced by the radiative heating has also been neglected. In the equation above, ρ is the density, c_p the specific heat, V the fixed volume beneath the applied heating (50 mm × 1.2 mm × 0.1 mm), $\overline{Q}_{abs}$ is the average absorbed radiative power, $\dot{m}$ the mass flux through the control volume due to the basic state velocity profile, and $(\overline{T}_{out} \overline{T}_{in})$, the average temperature rise of the fluid convected through the control volume. Using this result, one may calculate that, to effect a temperature change of $\Delta T = 0.5$ °C (the peak-to-peak variation observed at $Ma_L = 575$), the required peak radiative power, Q_{peak}, absorbed by the liquid layer should be about 25 mW. This is an extremely small value; in fact, it is two orders of magnitude below the applied aperture laser-power level of roughly 3 W employed in the control experiments.

ρ ∠ RHO

— ∠

$(\overline{T}_{out} - \overline{T}_{in})$, like

To further investigate this apparent discrepancy, an energy-balance experiment was performed for a 1 cS silicone-oil layer under the same conditions experienced by the liquid in the flow apparatus. An insulated liquid layer of volume $V = 10$ cm^3 was placed at the location normally occupied by the flow apparatus and exposed to the CO_2 laser sheet at a power level comparable to that employed for the control experiments ($P \approx 2.5$ W @ the laser aperture) for a period of 5 minutes. The change in the mean temperature of the layer following this exposure was $\Delta T \approx 0.9$ °C. Accounting for the optical losses in the experimental setup, it was estimated that the amount of energy reaching the free surface of the liquid is roughly 15% of the 2.5 W output by the laser. Therefore, of the roughly 110 J of energy incident upon the liquid layer, only 12.5 J were actually absorbed, indicating an absorption efficiency of 11%. Using the calculated absorption efficiency of 11%, the aperture laser power required to deliver the estimated peak absorbed radiative power of $Q_{peak} \approx 25$ mW is approximately $P_l \approx 1.5$ W, which compares reasonably well with the observed values of $P_l \approx 3.0$ W used in the control experiments.

It is interesting to note that the measured absorption efficiency of 11% for the 1 cS silicone oil is in contrast to the assumption made on the basis of results for 10 cS silicone oil, which Pline (1989) determined to be totally absorbing at a layer depth of 100 μm. Therefore, the smear sample of the 1 cS silicone oil shown in figure 4 probably provides a correct picture when it indicates that the 1 cS silicone oil used in these experiments is not very absorptive at the 10.6 μm spectral line corresponding to the laser output.

From the experimental results, one observes that excellent control of the hydrothermal waves is achieved with an output voltage to the laser of 3 V zero-to-peak (see, e.g. figure 7*c*). Using the efficiency calculated above, the power absorbed in the fluid layer for this output voltage is roughly 50 mW. This flux is approximately ten times that calculated as necessary to erase the hydrothermal-wave free-surface temperature depression.

4. Conclusions

The experiments described above have demonstrated the feasibility of suppressing oscillatory thermocapillary convection in thin liquid layers subject to a horizontal temperature gradient. Based upon the instability mechanism suggested by Smith (1986), control was achieved by heating troughs of low disturbance temperature with a sheet of IR radiation. The active feed-forward control scheme employed in these experiments is conceptually simple but effective for the suppression of hydrothermal waves in a high-Prandtl-number liquid.

Two features of the described experiments were key to their success: (i) the non-intrusive sensing of the surface-temperature fluctuations using an infrared camera; and (ii) the real-time determination of the hydrothermal-wave phase speed, allowing the control input to be precisely tailored to each hydrothermal wave. Earlier attempts at control by Riley (1995) using a thermocouple inserted below the free surface of the liquid achieved limited success due to the reliance on a single-point measurement and, perhaps, to the intrusive nature of the thermocouple inserted through the liquid free surface. The manual adjustment of the phase and amplitude of the forcing in those experiments made it impossible to suppress the oscillations for more than a few cycles.

There remain questions regarding the effectiveness of the CO_2 laser in providing surface heating to the 1 cS silicone oil employed for these experiments. Clearly, the laser is sufficiently powerful to accomplish the task, but the precise depth range of the applied heating is still unknown, as is the importance of this range. The work of Smith (1986) implies that, for high-Prandtl-number liquids, surface-temperature disturbances are coupled, through a convective process, to thermal disturbances in the bulk to sustain the instability. Hence, heating supplied to the bulk as well as to the surface may also provide a means of breaking this coupling.

Finally, the eventual use of such a technique in suppressing oscillations occurring during the float-zone crystal-growth process requires additional thought. First, such crystal-growth situations involve liquid metals of extremely small ($O(10^{-2})$) Prandtl number, so that the mechanism of the instability is different, as observed by Smith (1986) for planar layers and later by Levenstam & Amberg (1995) for a cylindrical geometry. In the planar case, hydrothermal waves propagate transversely across the layer, normal to the mean temperature gradient, meaning that the elimination of oscillations at the cold wall (solidification front) would require the simultaneous suppression of waves in the entire layer. For a cylindrical geometry exhibiting relatively few waves propagating in the azimuthal direction, this may or may not be possible.

We wish to thank Professor D. F. Jankowski for originally suggesting the idea of suppressing hydrothermal waves, Professor M. K. Smith for helpful discussions regarding the instability mechanism, Professor M. Yoda for assistance with the sheet-formation optics and colleagues in the School of Chemistry and Biochemistry at the Georgia Institute of Technology for performing the smear-sample spectrum shown in figure 4. Finally, we express our deep appreciation to Professor D. Schwabe for allowing Messrs. Benz and Hintz to each spend six months in Atlanta working on this project. This work was supported by the Microgravity ~~Science and Applications~~ Division, Office of Life and Microgravity Science and Applications of NASA. Additional travel funds were provided by DARA under contract number 50 WM 9446.

Research /

REFERENCES

GATOS, H. C. 1982 Semiconductor crystal growth and segregation problems on earth and in space. In *Materials Processing in the Reduced Gravity Environment of Space* (ed. G. E. Rindone) Elsevier.

LEVENSTAM, M. & AMBERG, G. 1995 Hydrodynamical instabilities of thermocapillary flow in a half-zone. *J. Fluid Mech.* **297**, 357.

LIEPMANN, H. W., BROWN, G. L. & NOSENCHUCK, D. M. 1982 Control of laminar-instability waves using a new technique. *J. Fluid Mech.* **118**, 187.

LIEPMANN, H. W. & NOSENCHUCK, D. M. 1982 Active control of laminar-turbulent transition. *J. Fluid Mech.* **118**, 201.

NAHAS, N. M. & PANTON, R. L. 1990 Control of surface tension flows: instability of a liquid jet. *Trans ASME J. Fluids Engng.* **112**, 296.

NEITZEL, G. P., LAW, C. C., JANKOWSKI, D. F. & MITTELMANN, H. D. 1991 Energy stability of thermocapillary convection in a model of the float-zone crystal-growth process. II: Nonaxisymmetric disturbances. *Phys. Fluids* A **3**, 2841.

PETROV, V., SCHATZ, M. F., MUEHLNER, K. A., VANHOOK, S. J., MCCORMICK, W. D., SWIFT, J. B. & SWINNEY, H. L. 1996 Nonlinear control of remote unstable states in a liquid bridge convection. *Phys. Rev. Lett.* **77**, 3779.

PLINE, A. D. 1989 Infrared surface temperature measurements for the surface tension driven convection experiment. *NASA* TM-101353 NASA Lewis Research Center.

RILEY, R. J. 1995 An investigation of the stability and control of a combined thermocapillary-buoyancy driven flow. PhD Thesis, Georgia Institute of Technology.

RILEY, R. J. & NEITZEL, G. P. 1998 Instability of thermocapillary-buoyancy convection in shallow layers. Part 1. Characterization of steady and oscillatory instabilities. *J. Fluid Mech.* **000**, 000–000.

SHEN, Y., NEITZEL, G. P., JANKOWSKI, D. F. & MITTELMANN, H. D. 1990 Energy stability of thermocapillary convection in a model of the float-zone crystal-growth process. *J. Fluid Mech.* **217**, 639.

SMITH, M. K. 1986 Instability mechanisms in dynamic thermocapillary liquid layers. *Phys. Fluids* **29**, 3182.

SMITH, M. K. & DAVIS, S. H. 1983 Instabilities of dynamic thermocapillary liquid layers. Part 1. Convective instabilities. *J. Fluid Mech.* **132**, 119.

TANG, J. & BAU, H. H. 1993 Stabilization of the no-motion state in Rayleigh-Bënard convection through the use of feedback control. *Phys. Rev. Lett.* **70**, 1795.

WANSCHURA, M., SHEVTSOVA, S., KUHLMANN, H. C. & RATH, H. J. 1995 Convective instability mechanisms in thermocapillary liquid bridges. *Phys. Fluids* **7**, 912.

⊙/

?hL